Eumelanin-Enhanced Photothermal Disinfection of Contact Lenses Using a Sustainable Marine Nanoplatform Engineered with Electrospun Nanofibers

Published Version:
Bartolewska, M., Kosik-kozioł, A., Korwek, Z., Krysiak, Z., Montroni, D., Mazur, M., et al. (2025). Eumelanin-Enhanced Photothermal Disinfection of Contact Lenses Using a Sustainable Marine Nanoplatform Engineered with Electrospun Nanofibers. ADVANCED HEALTHCARE MATERIALS, 14(2), 1-21 [10.1002/adhm.202402431].

Availability:
This version is available at: https://hdl.handle.net/11585/1051289 since: 2026-02-27

Published:

DOI: http://doi.org/10.1002/adhm.202402431

Eumelanin-Enhanced Photothermal Disinfection of Contact Lenses Using a Sustainable Marine Nanoplatform.

*Magdalena Bartolewska, Alicja Kosik-Kozioł, Zbigniew Korwek, Devis Montroni, Maciej Mazur, Giuseppe Falini and Filippo Pierini**

M.Bartolewska, Dr. A.Kosik-Kozioł, Dr. Z Korwek, Prof. F. Pierini
Department of Biosystems and Soft Matter, Institute of Fundamental Technological Research, Polish Academy of Sciences, Warsaw, 02-106, Poland
E-mail: fpierini@ippt.pan.pl

Prof. M. Mazur
Department of Chemistry, University of Warsaw, Warsaw, 02-093, Poland

Dr. D. Montroni, Prof. G. Falini
Dipartimento di Chimica "G. Ciamician", Alma Mater Studiorum—Università di Bologna, via F. Selmi 2, 40126 Bologna, Italy

Keywords: Photothermal disinfection, Contact lenses, LED light-activation, Marine-derived nanoplatforms, Mussel shells, Chitin nanofibrils

Abstract:

Bacterial keratitis (BK) is a severe eye infection commonly associated *with Staphylococcus aureus*, posing a significant risk to vision, especially among contact lens wearers. This research introduces a novel smart nanoplatform (deMS@cNF), developed from demineralized mussel shells and reinforced with chitin nanofibrils, specifically designed for portable photothermal disinfection of contact lenses. The nanoplatform leverages the photothermal properties of eumelanin in mussel shells, which, when activated by a simple bike flashlight, rapidly heats to temperatures up to 95°C, effectively destroying bacterial contamination. *In vitro* tests demonstrate that the nanoplatform is biocompatible and non-toxic, making it suitable for medical applications. This study highlights an innovative approach to converting marine biowaste into a safe, effective, and low-cost portable method for disinfecting contact lenses, showcasing the potential of the deMS@cNF platform for broader antimicrobial applications.

1. Introduction

Bacterial keratitis (BK) is a common ocular infection that is one of the most threatening to vision.[1] *Staphylococcus aureus* (*S. aureus*), a gram-positive bacteria, plays a significant role in causing bacterial keratitis, making up a significant portion of the reported cases globally.[1,2] After cataracts, this disorder ranks among the most common causes of blindness, with 12-66% of ocular diseases attributed to contact lens contamination.[3] Contact lens surfaces provide favorable growth conditions for bacteria due to their hydrophilic nature and organic deposits from tears.[3–5] Other factors such as hand hygiene, the type of lens care solution used, and accidental contamination of lens cases can also increase the risk of bacterial growth.[1]

Current contact lens disinfection practices rely mainly on chemical solutions containing hydrogen peroxide, chlorhexidine, or polyquaternium-1.[6] While these contact lens solutions meet the international ISO 14729 and FDA criteria for antimicrobial efficacy to reduce BK risk, concerns remain about their effectiveness against various clinical strains and biofilms formed on lenses.[7,8] Several studies have been published concerning the corneal toxicity of contact lens solutions and have reported that some formulations cause corneal staining *in vivo* and affect cell cultures, indicating cytotoxicity.[9] To address the limitations of current disinfection practices, researchers have been exploring alternative approaches for effectively and safely disinfecting contact lenses. UV light below 280 nm (UV-C) is an effective disinfectant for contact lenses but has drawbacks, such as the use of toxic mercury in light bulbs and potential damage to lens materials.[10] New UV LEDs are an alternative but remain costly, inefficient, and potentially dangerous. Visible light, particularly in the violet and blue spectrum, is less harmful and retains antimicrobial properties.[10,11] Hoenes et al. tested the combination of disinfectants with visible violet light of 405 nm for contact lens disinfection.[11] They found that the combination of contact lens disinfection solutions with the application of visible light irradiation could provide the same antimicrobial results as commercially available disinfection systems but with much less toxicity.[11]

Photothermal therapy (PTT) is a promising technique for antimicrobial treatment, which relies on the conversion of light into heat. In this method, a photothermal agent (PTA) absorbs light from an irradiation source and generates heat, which then eradicates pathogens by disrupting cellular structures and denaturing biomolecules like proteins and DNA.[12] It offers quick treatment and prevents bacterial resistance while delivering more effective broad-spectrum disinfection compared to traditional antibacterial methods.[12] Since photothermal disinfection of surfaces provides heat-based eradication, it can inactivate other pathogens, such as viruses, which makes this method a promising tool for a broad range of antimicrobial applications. [12,13] One new direction of scientific inquiry in this area is the exploration of marine-derived photothermal materials. Every year, large amounts of marine biomass waste are generated around the globe. In the seafood industry, 6–8 million tons of crustacean shell waste (e.g., crab, mussel shells, squid, and shrimp) are produced yearly.[14,15] This waste contains valuable materials that can be repurposed, with chitin being one of the most abundant.[14,16] Chitin (CT), a naturally occurring biopolymer primarily derived from marine organisms, presents a valuable resource in biomaterial research due to its biocompatibility, biodegradability, and non-toxic nature.[16] CT primarily exists in three forms: α-chitin, β-chitin, and γ-chitin, each with unique physical and chemical properties; α-chitin is commonly found in crustacean shells, β-chitin is typically derived from squid pens, and γ-chitin is predominantly present in insect cocoons.[17] Electrospinning has emerged as a promising technique for producing chitin nanofibers, driven by interest in their exceptional mechanical properties.[18][19] However, challenges persist due to chitin's insolubility in water and most organic solvents.[20] Initially, chitin dissolution required toxic solvents, which limited scalability and sustainability.[19,21] Recent advances involve using chitin nanofibrils as fillers in polymer solutions, thus bypassing these solvent-related challenges. Dobrovolskaya et al. developed a green method for electrospinning chitin nanofibrils by creating composite chitosan nanofibers containing 20 wt% chitin nanofibrils and 10 wt% poly(ethylene oxide) (PEO).[22] Their subsequent research demonstrated that the presence of chitin not only facilitates the formation of nanofibers under an electric field but also significantly reduces defects.[23] Junkasem et al. incorporated chitin whiskers into as-spun poly(vinyl alcohol)/chitin (PVA/CT) whisker nanocomposite nanofibers, which increased the Young's Modulus by approximately 4–8 times compared to the neat as-spun PVA fiber mat.[24] An underexplored strategy is to derive chitin scaffolds through the demineralization of shells.[25,26] Mussel shells consist of about 95 wt% brittle aragonitic $CaCO_3$ and 5 wt% organic materials such as chitin.[25] The main use for the mussel shells is to produce calcium carbonate, which is utilized as a filtering agent, a component in concrete formulations, or an ingredient in drug manufacturing.[27,28] Another application involves grinding the shells into a powder to be used as a natural calcium source in poultry feed.[29] However, the production of chitin-based dressings from demineralized mussel shells has yet to become widely established. Only a few publications investigated the composition of demineralized mussel shells, showing their porous structure.[25,26,30,31] Song et al. analyzed a mussel shell–derived membrane with a multiscale-ordered structure for wound dressing. They investigated that the demineralized shell is a biocompatible membrane with a highly organized porous structure and successfully works as a wound dressing and restores a particular skin defect in rats.[25]

It's important to note that certain shell species exhibit melanin in their outer layers, presenting intriguing prospects for photothermal applications.[32] Melanin is a polyphenolic compound with an anthracene ring as its monomer unit; it causes brown, black, and gray coloration in plants, microorganisms, and animals, as well as in the skin, hair, and eyes of humans.[33] Recently, melanin nanoparticles (MNPs) have garnered attention in nanomedicine for (PTT).[34] While most natural MNPs used for PTT are derived from cuttlefish ink,[35–39] the extraction and utilization of melanin from mussel shells remain relatively unexplored. Liu et al. successfully extracted melanin from mussel shells *Mytilus edulis*, and demonstrated its efficacy against pathogenic bacteria under near-infrared light.[40] These findings highlight the potential of mussel shells as a novel photothermal nanoplatform for eliminating bacterial infections.

This study aims to combine traditional biomaterials with innovative nature-derived materials by leveraging the unique properties of β-chitin from squid pens and melanin from mussel shells. We developed a smart multifunctional nanoplatform (deMS@cNF) composed of demineralized mussel shells (deMS) coated with crosslinked chitin-enhanced nanofibers (cNF). We examined the chemical, morphological, and mechanical properties of the nanoplatform to confirm the integration of β-chitin nanofibrils into PVA/PEO nanofibers and the integrity of the demineralized mussel shell structure. Following this, we evaluated the photothermal properties of the deMS@cNF under flashlight irradiation. *In vitro* assessments were conducted to explore the biocompatibility of the deMS@cNF nanoplatform, highlighting its potential for biomedical applications, particularly in contact lens disinfection. The ability of deMS@cNF to eradicate *S. aureus* on contact lenses was also tested, demonstrating its effectiveness under flashlight irradiation. This study underscores the successful valorization of marine biowaste into a multifunctional deMS@cNF nanoplatform, which opens new possibilities as a photothermal material. It exhibits excellent biocompatibility and on-demand portable antibacterial activity, making it suitable for applications that require disinfection of contact lens surfaces.

2. Results and Discussion

This study focuses on developing a multifunctional nanoplatform for disinfection of contact lenses (**Figure 1**). The core material for this platform is the organic matrix, also known as conchiolin, extracted from the shells of the blue mussel, *Mytilus edulis*. The outer layer consists of PVA/PEO nanofibers that are enhanced with β-chitin derived from squid pen (Figure 1a).

The product can be administered topically to cover contaminated contact lenses that can lead to bacterial keratitis, facilitating the antibacterial system with a use of a flashlight (Figure 1b).

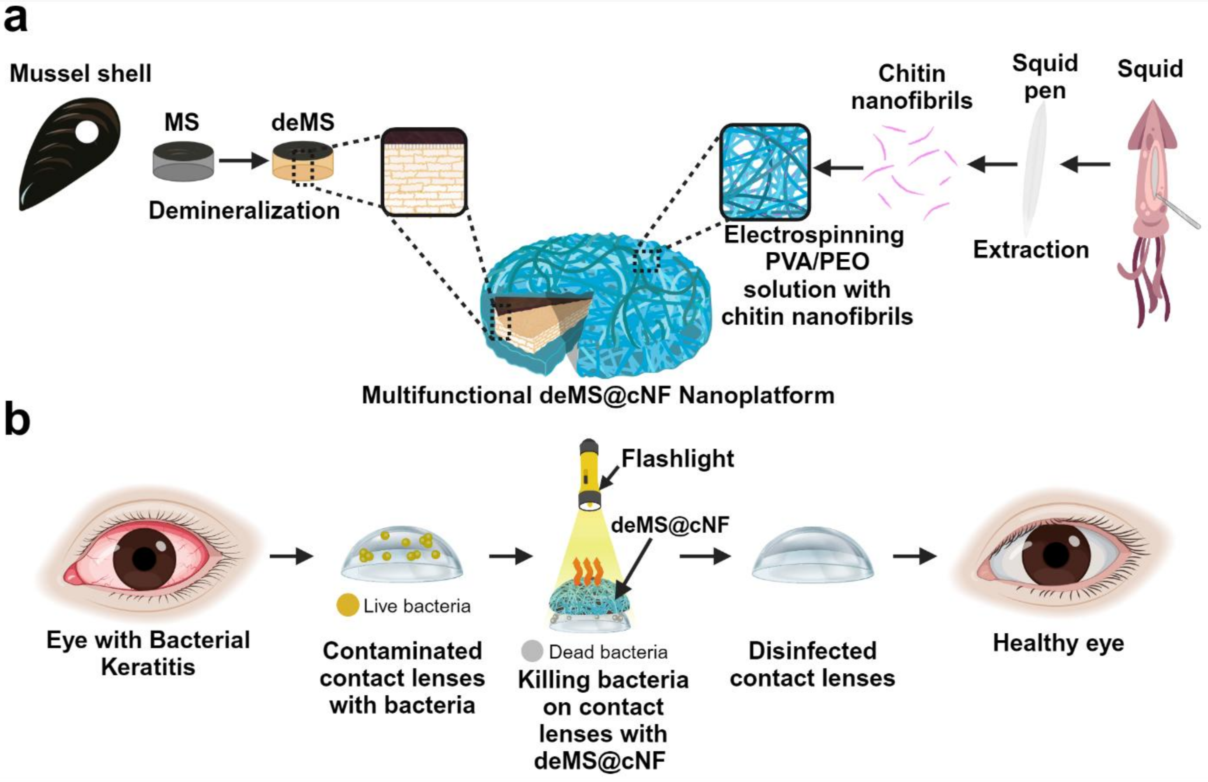

Figure 1. Illustration representing the development of the smart multilayer deMS@cNF nanoplatform and its application. a) Diagram of preparing the multifunctional deMS@cNF nanoplatform from mussel shell and squid. b) Schematic representation of a novel system for disinfection of contact lenses, using the multifunctional deMS@cNF nanoplatform.

2.1. Demineralization of mussel shells

Obtaining conchiolin involves a critical step called demineralization, which removes the mineral components of the shell. For this purpose, we employed a method using the EDTA solution, as described by Ehrlich et al.[26] This method was chosen specifically because it preserves the native structure of the organic matrix proteins within the shell. Harsh demineralization techniques, such as using hydrochloric acid (HCl), can damage the intricate architecture of the shell and compromise the integrity of the desired conchiolin material.[31]

The demineralization process of obtaining conchiolin from *Mytilus edulis* shells involves several key steps. First, the mussel shells were cleaned with deionized water (diH_2O) to remove any surface impurities. Subsequently, the shells were cut into round pieces (with diameter ~12 mm and thickness ~ 0,77 mm), in order to cover the contact lenses for disinfection. The prepared shell pieces were briefly submerged in an EDTA solution with a controlled pH of 7.25 for a duration of 24 hours. After this initial immersion, the shell pieces were thoroughly rinsed with

diH_2O water. This rinsing step removed any residual EDTA solution from the demineralization process. Following the rinsing, the shell pieces were immersed in a new EDTA solution. This cycle of soaking in EDTA solution, rinsing with water, and re-immersing in a new solution was repeated until complete demineralization of the shell was achieved (**Figure 2a**). During the demineralization process, as minerals were progressively removed, the material changed from a hard shell to a softer, more flexible form (Figure 2b). The demineralized shell began to shrink after being removed from the water, and by day 7, it was noticeably no longer flat. Additionally, the outer surface of the shell retained a black-brownish color, while the inner surface changed from a blue tint to a semi-transparent yellow as a result of demineralization (Figure 2b).

The shells of marine mollusks consist of three layers,[31,41,42] as depicted in the illustration in Figure 2a. The outermost layer, the periostracum (PL), is an organic layer composed of insoluble proteins with a thickness of approximately 14 µm (Figure 1S).[42] This layer protects the shell from the ocean environment while supporting the growth of calcium carbonate crystals in the shell's inner layers. The surface of the periostracum, both before and after demineralization, displays visible growth lines as shown in SEM (Figure 2c, PL upside-down triangle). The middle layer, known as the prismatic layer (PRL), consists of prismatic crystals of calcium carbonate (calcite) arranged obliquely to the shell surface (Figure 2c, PRL).[42] These calcite crystals consist of columnar prisms about 2 µm thick, polygonal in section and up to 50 µm long, arranged in sheet-like rows, and embedded within an organic matrix composed of proteins and chitin.[43] The prismatic layer is the thickest part of the shell, measuring approximately 250 µm. (Figure S1). The SEM images illustrate changes in the arrangement of calcium carbonate crystals and their connection to the nacreous layer (Figure 2c). They are attached through pallial myostracum (MB) that consists of irregular aragonite prisms and separates the calcitic and nacreous layers (Figure 2c, MB). This structure is relatively thin about 4 µm and is therefore considered as a band rather than a distinct shell layer.[41,42,44,45] The innermost layer, known as the nacreous layer (NL), contains flat crystals of aragonite, a polymorphic form of calcium carbonate. (Figure 2c, NL). These flat aragonite crystals, measuring about 0.5 µm in thickness and ranging from 5 to 15 µm in width, are aligned parallel to the shell surface and are also embedded within the organic matrix.[42,46] The thickness of NL layer can vary, ranging from very 90 µm up to 120 µm (Figure S1). The inner side of the shell reveals the formation of new aragonite tablets (Figure 2c, NL pink triangle).[47][42]

The shell structure undergoes significant changes in the prismatic layer (dePRL) and nacreous layer (deNL) following the demineralization process. The connection between the periostracum layer (dePL) and the dePRL forms holes (Figure 2c, dePL, dePRL). Additionally, the prismatic layer and the nacreous layer are not well attached to each other due to the demineralization of the myostracum band (deMB), resulting in the loss of their connection. After demineralization, the nacreous layer (deNL) exhibits porosity, which is only visible in SEM images of the deNL after lyophilization (Figure 2c, deNL, blue square). However, SEM images of the dePL, dePRL, and deNL samples dehydrated using ethanol reveal no visible porosity. This is attributed to the ethanol dehydration method, which failed to maintain the structural integrity of the porous network, resulting in its collapse upon drying (Figure 2c, dePL, dePRL, deNL, blue circle).

Post-demineralization, the initial mass of the mussel shell significantly reduces, as demonstrated in Figure 2d. The mussel shell retains only 4.5% of its total mass after demineralization.

The water contact angle test was performed on both MS and deMS surfaces of mussel shells, specifically targeting the inner area of the shell (NL). Results indicated that the NL of *Mytilus edulis* exhibited an average contact angle of 89.5 ± 0.7°, suggesting its hydrophobic nature (Figure 2d). This finding is consistent with previously reported values for mussel shells.[47] The deNL surface, primarily made of the organic matrix chitin, exhibited hydrophilic properties. As shown in Figure 2e, the water contact angle of the deNL surface was approximately 18.7 ± 2.1°.

The Raman spectrum of the prismatic and nacre layer from mussel shell (PRL+NL)MS revealed two lattice modes at 155 and 206 cm^{-1} and two internal modes at 704 and 1085 cm^{-1} (Figure 2f), which are consistent with aragonite characteristics.[48,49] These specific peaks are absent in the prismatic and nacre layer from demineralized mussel shell (PRL+NL)deMS, indicating complete demineralization. Additionally, polyene-related Raman peaks at 1105 and 1486 cm^{-1} are present across all layers, although their intensity varies after the demineralization process.[50] Measurements of both (PRL+NL)MS and (PRL+NL)deMS used a 514 nm laser. However, measuring the periostracum layer from the demineralized mussel shell ((PL)deMS) was challenging due to high fluorescence, which was resolved by switching the excitation laser to 738 nm. This adjustment reveals in two high-intensity polyene-related Raman peaks in (PL)deMS shown in Figure 2f.[50]

Structural analysis of the mussel shell composition was performed using attenuated ATR-FT-IR, both before and after demineralization (Figure 2g). (PRL+NL)MS spectra displayed characteristic peaks corresponding to crystalline calcium carbonate polymorphs. Notably, distinct bands were observed at 721 cm^{-1}, indicative of symmetric bending (ν4 mode), and at 874 cm^{-1}, corresponding to asymmetric bending vibrations (ν2 mode) of the carbonate ion (CO_3^{2-}). The symmetric bending vibration (ν1 mode) of the CO_3^{2-} group appeared at 1083 cm^{-1}, and the asymmetric bending vibration (ν3 mode) of the CO_3^{2-} group was noted at 1457 cm^{-1}.

[46,51] (PRL+NL)deMS spectra in the range of 834-899 cm^{-1} show stretching vibrations of C-O-C and C-C bonds, typically associated with α-chitin.[51,52] Between 1100-1700 cm^{-1}, multiple bands were evident, predominantly corresponding to the amide bands (I, II, and III) of proteins, which include vibrations of C=O, C-N, N-H, and C-C, as well as α-chitin vibrations (CH_2, OH, and C=O). The amide III region at 1383 cm^{-1} demonstrated a combination of vibrations involving N-H bending, C-N stretching, and C-H bending. The amide II region at 1594 cm^{-1} was characterized by N-H bending and C-N stretching vibrations. At 1635 cm^{-1}, the amide I region showed prominent C=O stretching vibrations. [46,51,53]

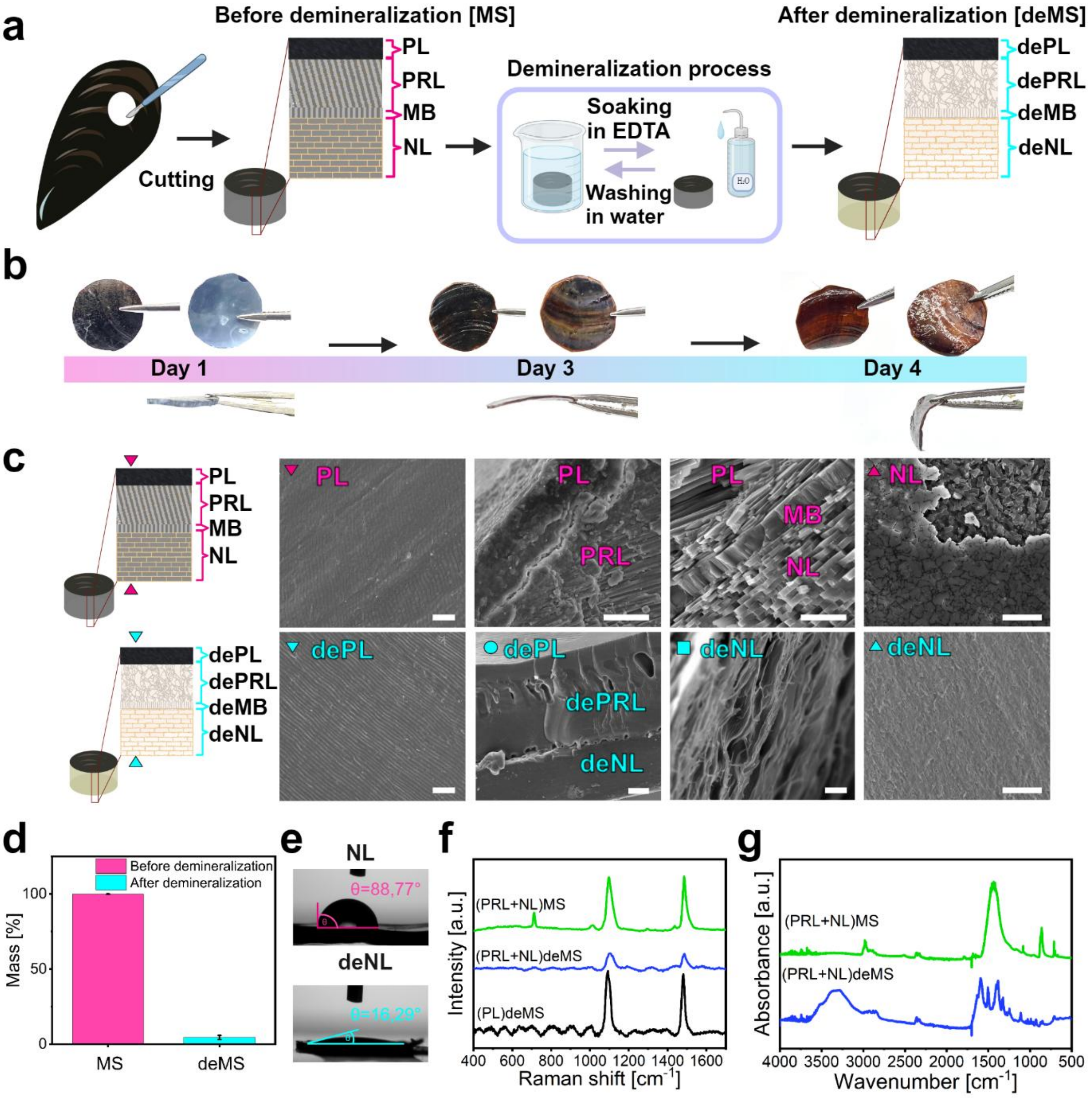

Figure 2. Schematic representation and effective evaluation of the mussel shell demineralization process. a) Illustration of the demineralization process. b) Sequential photographs of the mussel shell during the demineralization stages. c) SEM images illustrating the microstructure of different parts of the mussel shell before (pink) and after (blue) demineralization; scale bar: 10 µm. d) Mass loss resulting from the demineralization e) Contact angle measurements on mussel shell inner surfaces before demineralization (NL) and after demineralization (deNL), depicting changes in hydrophobicity. f) Raman spectra highlighting changes in the mussel shell pre- and post-demineralization. g) ATR-FT-IR spectroscopy of the mineral part of the mussel shell before (PRL+NL)MS and after demineralization (PRL+NL)deMS, showing changes in functional group absorption peaks. Abbreviation: periostracum layer (PL), prismatic layer (PRL), myostracum band (MB), nacre layer (NL), mussel shell (MS), demineralized (de).

2.2. Characterization of electrospun PVA/PEO nanofibers filled with chitin nanofibrils

Inspired by the structural and mechanical properties of chitin nanofibrils in the squid pen, we explored incorporating them into a PVA/PEO solution via electrospinning, as illustrated in **Figure 3a**.[54] First, chitin nanofibrils were obtained through the deproteinization of squid pen (Figure 3b), sourced from squid *Loligo vulgaris*.[55] These nanofibrils were then reduced to smaller pieces and subsequently dispersed in acetic acid, as depicted in Figure 3a. For integration into the polymer nanofibers, a concentration of 0.1% chitin nanofibrils dispersed in acetic acid was utilized. The size of the chitin nanofibrils was previously reported by Monroni et al., who identified two main groups: one with a maximum average length of 160 ± 50 nm and the other with 340 ± 150 nm, both having a height of 2.5 ± 0.3 nm. The prepared solution was briefly loaded into a syringe equipped with a 22 G needle, and a high voltage of 16 kV was applied. With a flow rate of 400 µL/h, the fibers began to form and were collected on a flat collector, as shown in Figure 3a.

Characterization of the chitin nanofibrils was conducted. X-ray diffraction (XRD) analysis confirmed the presence of chitin as the β polymorph (Figure 3c). Peaks at 8.6° correspond to the crystal plane (010), while peaks at 19.6° correspond to $[1\bar{1}0]$ reflection value.[55–57] Comparisons with existing literature confirm that the native β-chitin structure was maintained throughout the process of nanofibril isolation.[55,56,58]

The FT-IR spectra of the isolated β-chitin, shown in Figure 3d, closely match those in established literature, confirming the high quality of the obtained chitin.[55,56,59,60] Analysis reveals characteristic polysaccharide bands, including a broad band between 3600 and 3000

cm^{-1}, associated with the stretching vibrations of –OH and –NH groups. The spectrum also displays bands from 2961 to 2886 cm^{-1} indicative of CH, CH_3 symmetric stretching, and CH_2 asymmetric stretching.[60] The peak at 1654 cm^{-1}, characteristic of the Amide I band, confirms the presence of β-chitin, as it suggests hydrogen bonding interactions within and between chitin chains.[21,52,61] Additionally, the amide II and III bands are noted at 1554 and 1308 cm^{-1}, respectively.[60,62,63] The bands between 1163 and 1027 cm^{-1} are attributed to the asymmetric bridge oxygen and C–O stretching vibrations.[63] This detailed spectral analysis supports the high-quality extraction and structural integrity of the β-chitin.

In the introduction of our study, we address the prevalent challenges associated with electrospinning chitin. To harness the mechanical properties of chitin nanofibrils, we proposed a new method for incorporating β-chitin nanofibrils into a polymer solution. During the initial optimization of the electrospinning process for PVA with CT nanofibrils, we encountered significant technical challenges, such as frequent clogging of the electrospinning needle and the formation of beaded fibers (Figure S2). To address these issues, PEO was incorporated into the spinning solution. The addition of PEO significantly enhanced both the viscosity and the elongational viscosity of the solution, facilitating the production of uniform, bead-free nanofibers and ensuring a continuous and stable electrospinning process. These enhancements in fiber morphology and process reliability are substantiated by SEM analyses, which are detailed in the supplementary data (Figure S3). The positive impact of PEO on the electrospinning process is further supported by recent studies.[64,65]

To investigate the influence of chitin nanofibrils on the morphology and mechanical properties of nanofibers, three distinct solutions were prepared. Each solution featured a blend of PVA and PEO: the first dissolved solely in MilliQ water, the second in a MilliQ water and acetic acid mixture (AA), and the third in a combination of MilliQ water and a 0.1% chitin nanofibril suspension in acetic acid (CT). The nanofibrous mats from each solution underwent a crosslinking process, where they were immersed in ethanol for 24 hours, subsequently dried, and then thermally treated at 160°C. According to Zakrzewska et al., soaking in ethanol enhances crosslinking before crosslinking in temperature.[66] The effects of acetic acid and chitin nanofibrils on the nanofibers' morphology and mechanical properties were critically assessed. Additionally, the impact of the crosslinking process on these properties was evaluated. According to Figure 3e, which presents FE-SEM images, all solutions produced beadle-less and well-formed nanofibers. Significantly, the average diameter of the nanofibers demonstrated variability across treatments: for PVA/PEO, the diameter was 149 ± 42 nm ($n \geq 40$); upon addition of AA, the diameter increased to 196 ± 27 nm ($n \geq 40$); whereas with CT, the diameter slightly decreased to 169 ± 40 nm (n ≥ 40). Crosslinking generally doubled the diameter of PVA/PEO fibers to 290 ± 62 nm (n>40) while interestingly reducing the average diameter of PVA/PEO/AA fibers to 141 ± 38 nm (n>40). The inclusion of chitin nanofibrils (CT) after crosslinking showed a minimal diameter increase of about 13 ± 57.28 nm.

The Young's Modulus of electrospun nanofibers was assessed to determine their mechanical properties. The PVA/PEO nanofibers exhibited a Young's Modulus of 27.46 ± 0.25 MPa. When acetic acid was incorporated (PVA/PEO/AA), the modulus increased to 43.01 ± 1.22 MPa. Acetic acid is a frequently used solvent for electrospinning, and it has a positive impact on the preparation of nanofibers.[67] Vu et. al. showed that the use of AA as a solvent had no effect on the chemical properties of the prepared PVA nanofibers, and the mechanical strength of the PVA nanofibers increased with the concentration of AA in the electrospun solution.[68] Additionally, Stie et al. demonstrated that using AA as a solvent to produce chitosan/polyethylene oxide nanofibers that could be maintained in water for 4 h and still retain their shape and fibrous structure, whereas the use of succinic or citric acid as solvents resulted in the disintegration of chitosan/polyethylene oxide nanofibers mats after 4 h in water.[67] Notably, the addition of chitin nanofibrils (PVA/PEO/CT) significantly enhanced the Young's Modulus to approximately 73.03 ± 4.61 MPa, which is 2.7 times higher than that of the PVA/PEO nanofibers. The similar property was found by Junkasem et al., they have prepared chitin nanocrystal/PVA composite fibrous mats by electrospinning, confirming that Young's Modulus is 4-8 times higher than pure PVA mats.[24]

Following the crosslinking process, the Young's Modulus of the PVA/PEO nanofibers doubled to 51.33 ± 7.11 MPa. For the PVA/PEO/AA nanofibers, the modulus increased by approximately 2.6 times, reaching 110.66 ± 8.15 MPa. These significant enhancements in mechanical properties, especially the substantial increase in Young's Modulus following crosslinking of PVA/PEO/AA nanofibers, have not been previously documented for these specific nanofiber compositions. However, surprisingly, the Young's Modulus of the PVA/PEO/CT nanofibers decreased slightly post-crosslinking resulting in 61.77 ± 3.53 MPa. This reduction may be attributed to structural changes induced by the presence of chitin nanofibrils, suggesting an interaction between the polymer matrix and the nanofibrils that affects the mechanical integrity post-crosslinking.

To validate the incorporation of chitin into PVA/PEO nanofibers post-electrospinning, high-performance liquid chromatography (HPLC) was employed. Due to β-chitin's insolubility in water and most solvents, hydrolysis with acid, alkali, or enzymes was necessary to yield glucosamine for detection. The glucosamine release profile from hydrolyzed β-chitin was studied using the method reported by Zhu et al.[69] A glucosamine peak was observed in the electrospun PVA/PEO/CT nanofibers (Figure 5g). The chitin content in the PVA/PEO/CT nanofibers was estimated at 0.49%, while no peak was detected in the PVA/PEO nanofibers, indicating a CT content of zero (Figure 5h). This finding is particularly noteworthy, demonstrating that even a low CT content can enhance the mechanical properties of neat PVA/PEO nanofibers by 2.7 times.

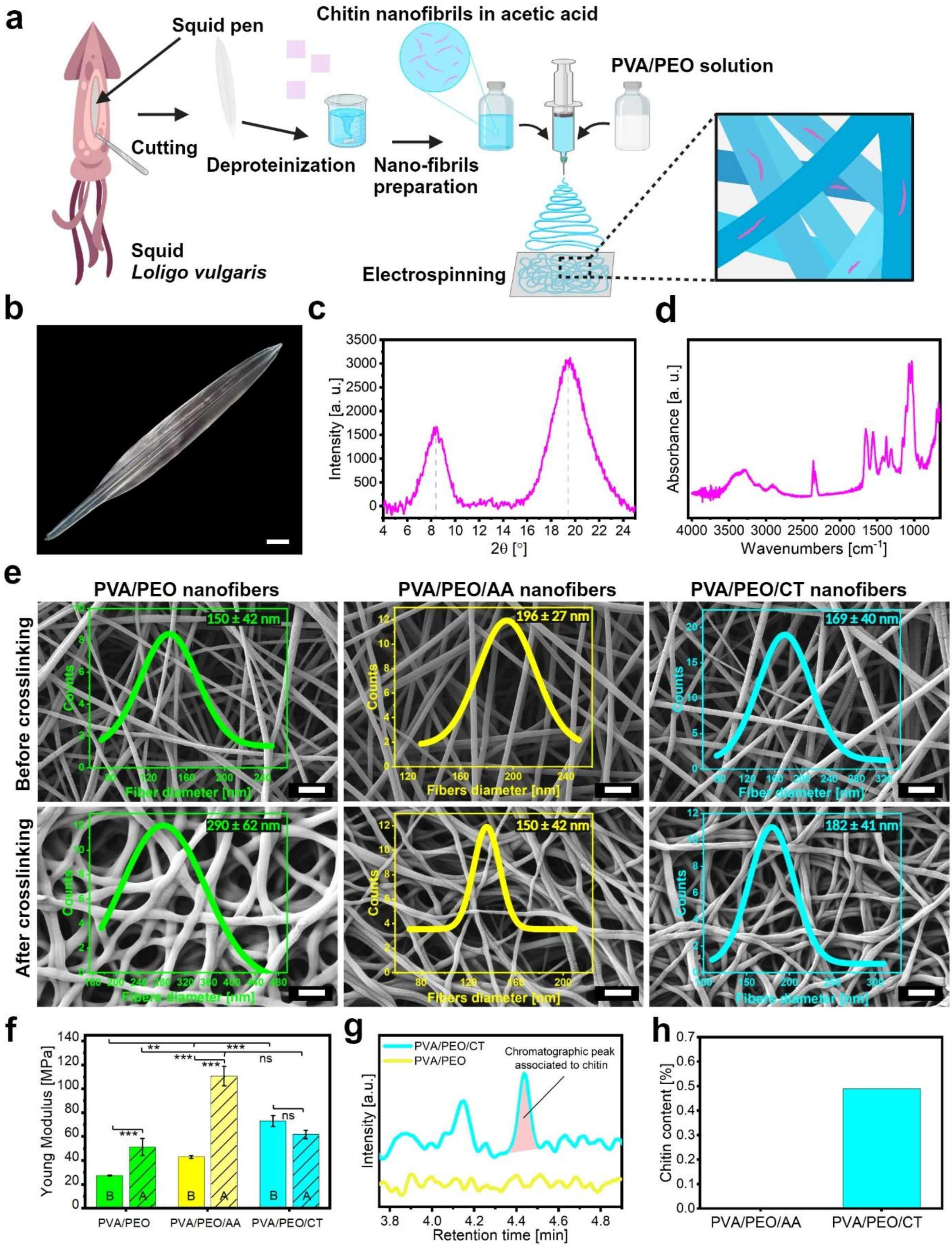

Figure 3. Chitin nanofibril isolation and their incorporation into electrospun nanofibers. a) Schematic representation of the process for extracting chitin from squid pens and its incorporation into the electrospinning process. b) Photograph of squid pen. Scale bar: 1 cm. c) XRD analysis of chitin nanofibrils, showing their crystalline structure. d) FT-IR spectra of chitin nanofibrils, detailing specific functional groups. e) SEM images displaying the

morphology of nanofibers before and after crosslinking for three formulations: polyvinyl alcohol/polyethylene oxide (PVA/PEO), PVA/PEO with acetic acid (AA), and PVA/PEO with chitin (CT). Scale bar: 1 µm f) Graph presenting the Young's Modulus of the nanofiber formulations, indicating differences in stiffness and flexibility. g) HPLC analysis of glucosamine peak associated with chitin, used to quantify the amount of chitin incorporated into the nanofibers. h) Chitin content in electrospun nanofibers for two formulations: PVA/PEO/AA, PVA/PEO/CT, indicating the effectiveness of chitin incorporation into the nanofibers.

2.3. Development and characterization of the multilayered light-responsive deMS@cNF nanoplatform

The next step in this research was to combine two materials: demineralized mussel shells and chitin enhanced PVA/PEO nanofibers. We proposed using the mussel shells as the core substrate of nanoplatform. To protect the demineralized shells, we decided to coat them with chitin-enhanced nanofibers, which possess strong mechanical properties essential for maintaining structural integrity (Figure 1a). To prepare the multilayered nanoplatform (deMS@cNF), the mussel shells were first cut into smaller round pieces with a diameter of 12 ± 2 mm (**Figure 4a**). These round-shaped pieces were then placed on a flat collector within the electrospinning chamber. Following the previously described method, a solution of PVA and PEO in water was prepared, to which chitin nanofibrils in AA were added. This solution was transferred to a syringe equipped with a 22G needle, and a voltage of 16 kV was applied, causing the solution to form nanofibers that collected on the MS. Spinning continued until the shells were coated on both sides with fibers (MS@NF). The next step involved crosslinking the nanofibers before the demineralization process. The porosity of the nanofibers facilitated the efficient demineralization of the mussel shells. Therefore, the nanofibers were pre-crosslinked by soaking the shell in ethanol for 24 hours, followed by drying in room temperature for 3 hours and heating at 160°C for 20 minutes. It was found that the crosslinking process at high temperatures affects the nacre layer before demineralization, as shown by the presence of small holes visible in the SEM images (Figure S4). After this preparation, the mussel shells covered with crosslinked nanofibers (MS@cNF) were ready for the demineralization process, which was the same as for the mussel shells not covered with fibers. They were soaked in EDTA at pH 7.25, with the solution changed daily until complete demineralization was achieved.

To verify the success of the process, the deMS@cNF were examined under SEM (Figure 4b). These crosslinked nanofibers withstood seven days of immersion in the EDTA solution (indicated by the blue arrow), remained intact, continuing to cover the demineralized mussel shells (Figure 4b). The core of multilayer nanoplatform is made of the demineralized shell; yellow arrows point to the demineralized nacre structure, orange arrows point to the demineralized prismatic layer, and red arrows highlight the periostracum layer (Figure 4b). As shown in Figure 4c, the demineralization time was very similar to that of the not covered shells. The mass loss was higher and more rapid in the shell-only samples. The shells covered with fibers showed slightly slower demineralization due to the barrier effect but were still successfully demineralized. Swelling ratios were also tested for the deMS and the deMS@cNF. The swelling ratio of deMS@cNF was higher, indicating that the nanofibers played a significant role in water retention (Figure 4d). Additionally, a dehydration test was conducted to compare these two materials (deMS and deMS@cNF). The deMS@cNF retained water slightly longer, beginning to dehydrate around 90 minutes after removal from water, while the untreated shells started to dry after just 40 minutes (Figure 4e).

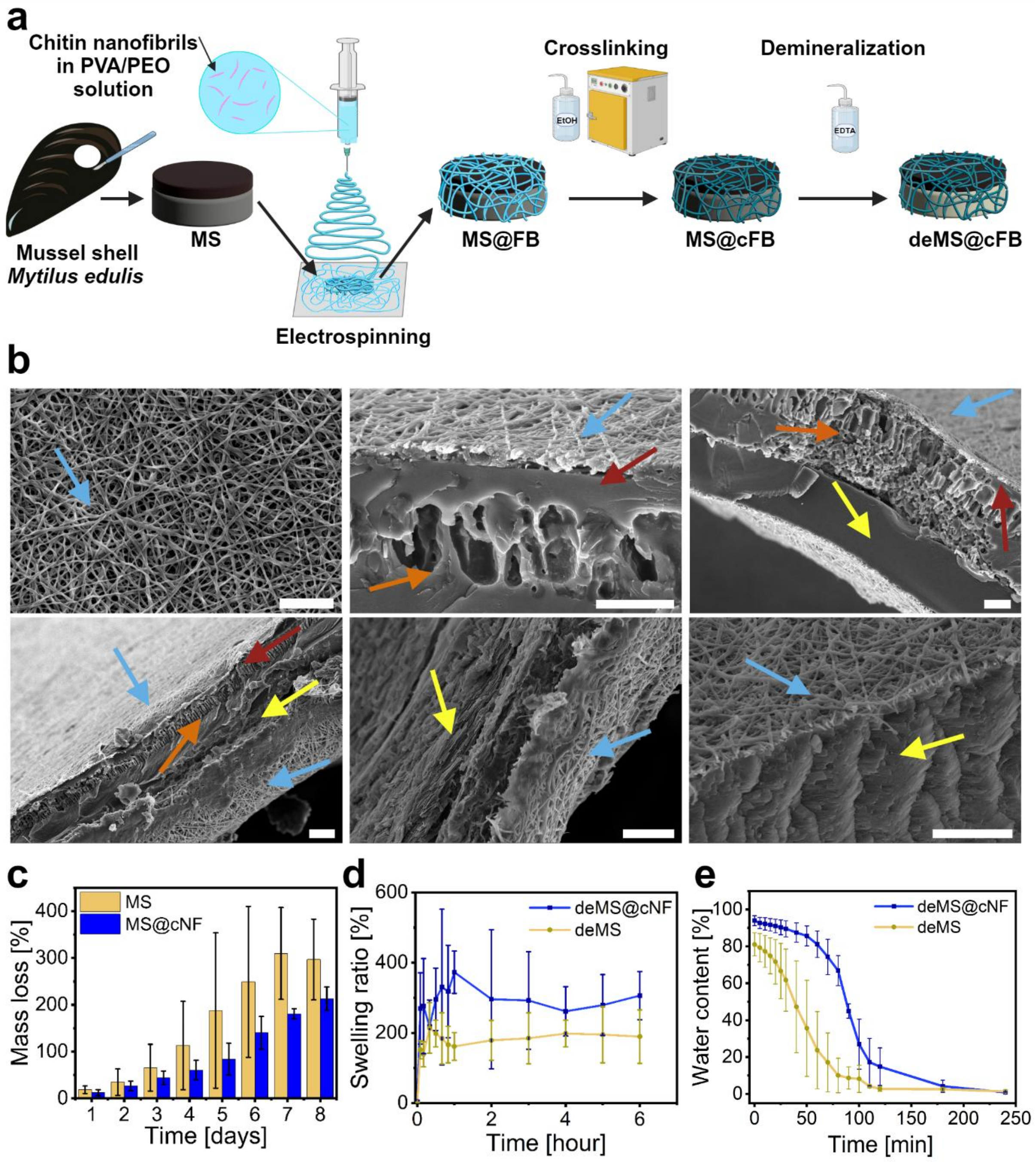

Figure 4. Characterization of the multifunctional nature-derived deMS@cNF nanoplatform a) Schematic illustration showing the steps involved in coating mussel shells (MS) with chitin-enhanced nanofibers (PVA/PEO/CT) to fabricate the demineralized mussel shells coated with nanofibers (deMS@cNF). b) SEM images of the cross-section of the multifunctional nanoplatform (deMS@cNF). Blue arrows indicate the nanofibers, yellow arrows point to the demineralized nacre structure, orange arrows point to the demineralized prismatic layer, and red arrows highlight the periostracum layer. c) Graph depicting the comparative mass and mineral loss during the demineralization process for both mussel shells (MS) and mussel shells coated with crosslinked PVA/PEO/CT nanofibers (MS@cNF).

d) Swelling ratio comparisons between demineralized mussel shells coated with nanofibers (deMS@cNF) and demineralized mussel shells (deMS). e) Comparison of the dehydration process for deMS and deMS@cNF.

2.4. Photothermal characterization

Eumelanin, a naturally occurring dark pigment that imbues color to human skin, hair, and eyes, is renowned for its exceptional light absorption capabilities across a broad spectrum, particularly in the ultraviolet (UV) and visible light regions.[70] This potent absorption is attributed to its chemically complex structure, which is rich in conjugated double bonds.[71] Unlike many pigments that merely reflect light, eumelanin excels in absorbing light and efficiently converting it into heat through a process known as non-radiative decay, positioning it as a promising photothermal agent.[71] A unique characteristic of eumelanin is its ability to convert absorbed UV radiation into heat in less than 1 nanosecond.[72]

Recent investigations have revealed the presence of eumelanin in the periostracum layer of the *Mytilus edulis* mussel shells, suggesting novel applications of eumelanin beyond traditional pigmentation roles.[32] Building on this discovery, our study introduces a deMS@cNF nanoplatform to evaluate its photothermal responsiveness under LED light irradiation. We used a bike flashlight as the irradiation source instead of a more conventional NIR laser or solar lamp. Utilizing a bike flashlight offers several benefits, primarily its accessibility and safety. Unlike NIR lasers or solar lamps, bike flashlights are inexpensive, widely available, and easy for anyone to obtain and use. This makes the experimental setup more practical and reproducible for a broader audience.[10,73]

Our experimental setup recorded the system's temperature response to varying bike flashlight powers and different distances between the material and sourced irradiation (**Figure 5a**). The temperature-time profiles demonstrated that temperature increases were rapid and directly proportional to the power of the flashlight, for all distances (Figure 5b). Thermal imaging supported these findings, showing the heat distribution across the material once a stable temperature plateau was reached (Figure 5b). Notably, the sample achieved a peak temperature of around 90°C when positioned 3 cm from a flashlight emitting 320 mW/cm^2. This optimal condition was subsequently evaluated for its antibacterial effectiveness in disinfecting contact lenses.

Figure 5c shows the spectrum of the LED bike flashlight used, which has two peaks: a sharp peak at 460 nm (blue) and a broad peak at 560 nm (green). Using a bike flashlight as a light source for photothermal applications, such as antimicrobial treatments, presents a practical and efficient alternative to NIR lasers or solar lamps.[74] Additionally, LED flashlight can be used as a source for photothermal materials that convert light into heat and kill bacteria. There are several papers about the effects of LED light on bacteria.[73,75–78] While red light or near-infrared light has been reported to exert no antimicrobial effects, blue light has been reported to possess bactericidal effects.[75,79] The delivery of blue light (representing 15–58.8 J/cm² energy density) is sufficient to reduce the viability of bacteria such as *H. pylori*, *methicillin-resistant S. aureus*, *P. aeruginosa*, and *S. aureus*.[75,77,80,81] Upon blue LED irradiation, endogenous porphyrin produced by bacteria is excited, leading to a photodynamic reaction through singlet oxygen production, thus resulting in bacterial killing.[75] However, it is still unclear whether exposure to blue LED kills or inhibits the growth of bacteria. Chui et.al reported that blue LED irradiation inhibited the growth of *P. gingivalis* by suppressing the expression of genes associated with chromosomal DNA replication and cell division at the transcriptional level.[75]

The repeated irradiation and cooling cycles, depicted in Figure 5d, demonstrated the material's capability to rapidly heat to temperatures between 80-95°C within five minutes and return to ambient temperature shortly after the pause of irradiation. This study not only underscores the robust photothermal properties of deMS@cNF but also opens potential avenues for using eumelanin-enhanced materials in various biomedical applications, particularly antimicrobial treatments. Research on the photothermal properties of eumelanin typically uses cephalopod ink as a source. Jia et al. and Kong et al. produced a hydrogel with exceptional photothermal properties using melanin nanoparticles (MNPs) from cuttlefish ink under NIR laser irradiation (1 W/cm²). Jia et al. reached a temperature of up to 63.6°C, while Kong et al. reached 55°C; both studies effectively eradicated *S. aureus* and *E. coli*. [35,39] Similarly, Cao et al. demonstrated the use of MNPs in hydrogels to enhance wound healing and provide antibacterial protection through photothermal effects. They utilized a laser power of 0.9 W/cm², achieving temperatures around 60°C, effectively eradicating *S. aureus* and *E. coli* bacterial colonies.[37] Lei et al. integrated MNPs into microneedle patches for simultaneous skin tumor photothermal therapy and wound healing. The applied laser power was 0.2 W/cm², achieving temperatures of approximately 73.2°C, eradicating *S. aureus* bacteria.[38] Liang et al. developed edible antibacterial food packaging films that achieved significant sterilization of *Listeria monocytogenes* under NIR irradiation, extending food shelf life. They used a laser power of 2 W/cm², reaching temperatures of 70°C.[36] While all the described studies used NIR lasers, our use of a white LED light source simplifies the experimental setup, making it more accessible and cost-effective, while achieving higher temperatures compared to those reached with NIR lasers (as shown in Figure 5e and detailed in Supplementary Table S1).

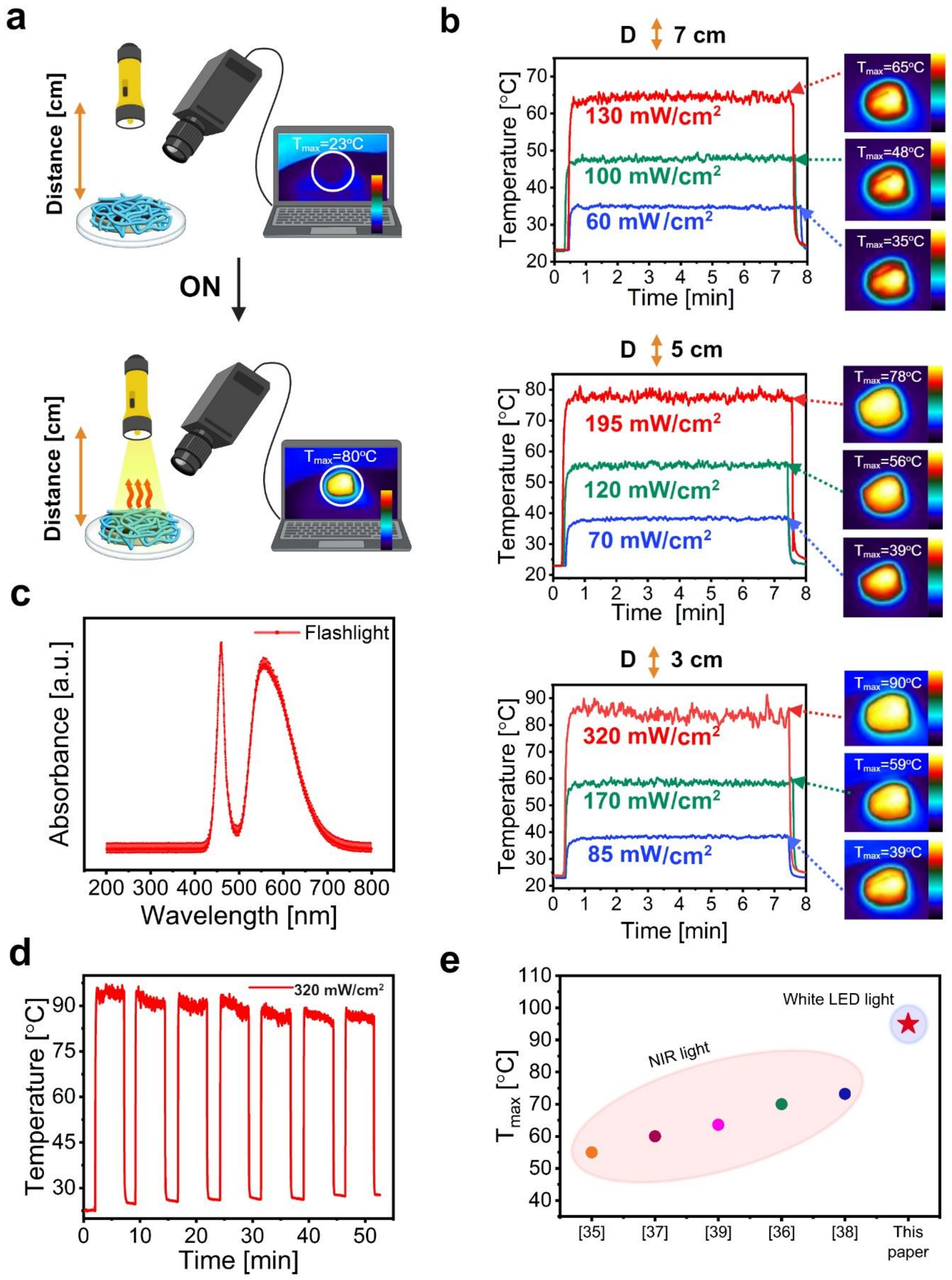

Figure 5. Evaluation of photothermal properties of the deMS@cNF platform. a) Schematic representation of the experimental setup for the photothermal testing, illustrating the configuration of the flashlight and the sample positioning. b) Graphs showing the temperature-time profiles and thermal images for the deMS@cNF composite at varying distances (D) between the flashlight and the sample to assess the influence of distance on photothermal efficiency. c) Spectra of LED flashlight d) Repeated cycle graph depicting the stability of temperature changes in the deMS@cNF over seven cycles of photothermal testing, highlighting the material's ability to sustain repeated photothermal activation e) Comparison of maximum temperature reached in the multifunctional nanoplatform using MNPs for bacterial eradication in this work to other papers.

2.5. *In vitro* cell biocompatibility studies

To evaluate the biocompatibility of the proposed multifunctional nanoplatform, interactions with L929 fibroblast cells were examined according to ISO 10993-12:2021 and ISO 10993-5. Initially, the biocompatibility assessment involved direct cell seeding assays on deMS@cNF. As a control, cells were seeded on slide glass (**Figure 6a**). Over the course of seven days, not only did the L929 cells exhibit proper adherence to the deMS@cNF platform, but they also displayed noticeable progressive proliferation. Morphological evaluations, undertaken through SEM after a seven-day culture period, revealed that the cells adhered to the deMS@cNF substrates had adopted an elongated, spindle-like shape, indicative of the effective cellular support provided by the scaffolds (Figure 6b).

Furthermore, an indirect cell culture approach was employed to ensure that the influence of the material's surface structure was effectively eliminated, allowing for a focused investigation into the cellular interactions prompted by the substances released from the deMS@cNF, the step of the indirect method is demonstrated in Figure 6c. Figure 6d shows that cell growth and proliferation induced by extracts from deMS@cNF (Ex_deMS@cNF) are comparable to those observed in medium (DMEM supplemented with fetal bovine serum (FBS) and penicillin-streptomycin (P/S)). A Live/Dead assay was used, staining viable cells green and dead cells red. Images from the Live/Dead assay revealed a predominant presence of viable green cells on both day 3 and day 7 of the culture period, demonstrating the materials' cytocompatibility (Figure 6e). Furthermore, confocal microscopy was applied to analyze the morphology of the actin cytoskeleton and nuclei on days 3 and 7. The morphology of L929 cells exposed to extracts from deMS@cNF showed well-preserved intercellular connections. The cells maintained high viability with intact and healthy nuclei stained by DAPI, as shown in Figure 6f.

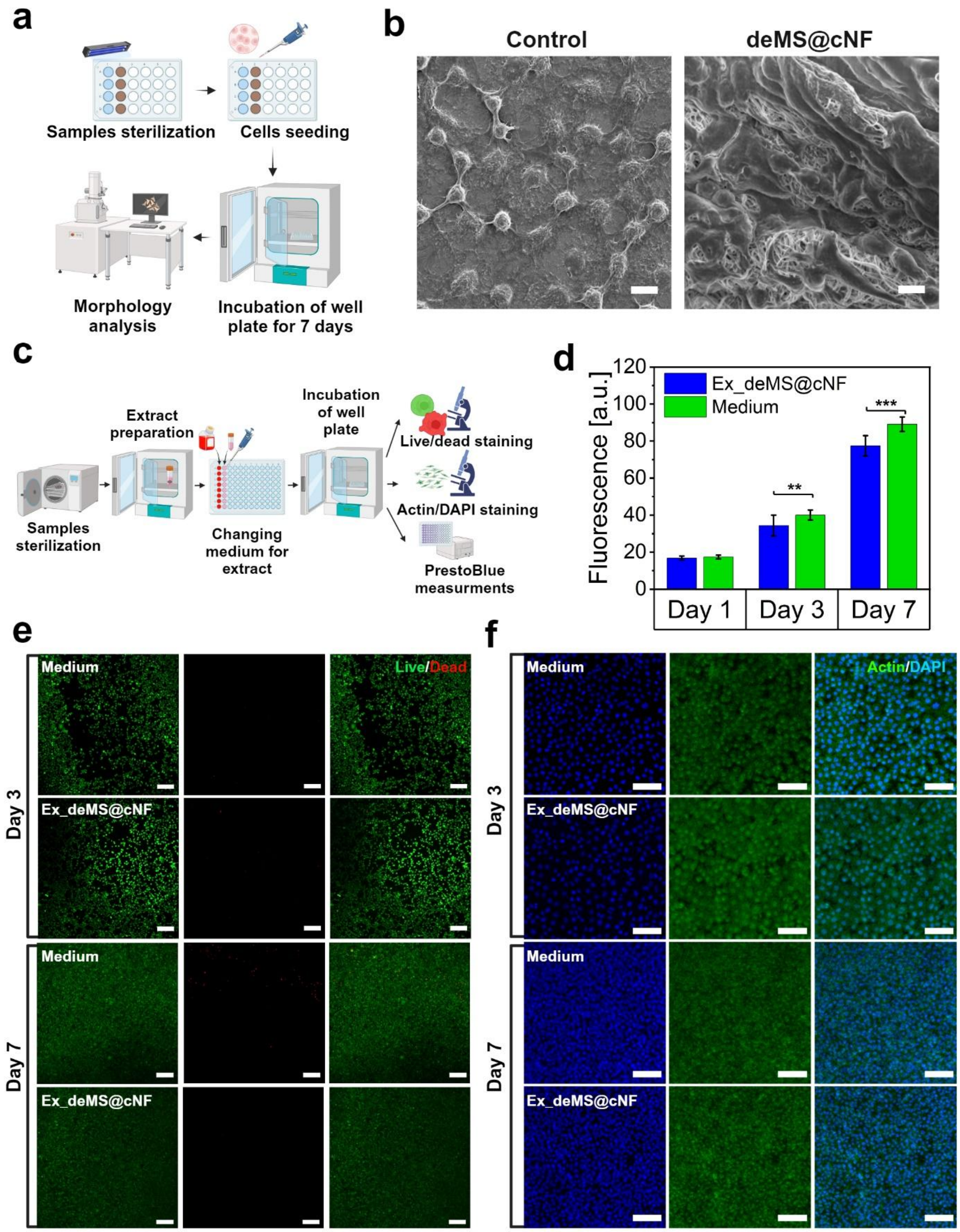

Figure 6. *In vitro* biocompatibility of the deMS@cNF nanoplatform. a) Graphic depiction of the sample preparation and experimental procedure for direct cell viability studies, detailing the steps involved in seeding and cultivating L929 cells on the deMS@cNF composite and control surfaces. b) SEM images of L929 cells cultured on deMS@cNF and control (glass slides) on day 7, showcasing cell morphology and adherence patterns. Scale bar equal to 10 µm. c)

Schematic illustration of the setup for indirect cell viability studies, using Ex_deMS@cNF (extracts from the deMS@cNF nanoplatform) and medium (DMEM+FBS+P/S). d) Graphs of cell fluorescence measurements on days 1, 3, and 7, quantifying L929 cell proliferation and viability using PrestoBlue assay e) Confocal microscopy images of Live/Dead staining on days 3 and 7 for indirect studies (green – live cells, red – dead cells). Scale bar equal to 200 µm. f) Confocal image (stained with DAPI for nuclei – blue, and Actin for cytoskeleton visualization – green) of L929 fibroblast on day 3 and day 7, features to assess cell health and morphology over time. Scale bar 100 µm.

2.6. *In vitro* light-activated antibacterial properties

Considering the prevalence of bacterial keratitis in patients who wear contact lenses, we explored the efficacy of the multifunctional nanoplatform (deMS@cNF) for bacterial eradication on contact lenses, using flashlight irradiation as the activation method. We specifically targeted *S. aureus*, a common bacterial contaminant found on contact lenses.[8] **Figure 7a** illustrates the application of the multifunctional nanoplatform (deMS@cNF) in effectively eradicating bacteria from the surface of contact lenses. Figure 7b provides an illustration of the agar plate used during the direct test, highlighting bacterial biofilm growth on samples before and after flashlight irradiation (+), both with (CL@D) and without (CL) deMS@cNF. There was a markedly lower growth of bacteria on agar areas imprinted with contact lenses treated with deMS@cNF and irradiated by flashlight (CL@D+) (Figure 7b). Conversely, areas imprinted with non-irradiated contact lenses (CL), both with and without deMS@cNF, showed unrestrained bacterial growth, completely covering the area with a bacterial lawn within 24 hours. Irradiated contact lenses without deMS@cNF (CL+) displayed only a mild antibacterial effect, supporting previous research that tested bacterial eradication on contact lenses using lens solution and 460 nm light, also found in the LED flashlight that we used.[73,81] However, using the flashlight alone was insufficient to effectively kill the bacteria. These findings were further supported through Live/Dead analysis of bacteria subjected to eradication process (Figure 7c). Contact lenses were stained using SYTO 9, which binds to DNA and visualizes bacteria, and with propidium iodide (PI) that stains dead bacteria (Figure 7c) [82] The treatment CL@D+ was efficient, with the red stain from dead bacteria clearly visible, indicating it high efficacy. The rest of the treatments showed mostly live bacteria, except for the samples where contact lenses were covered with deMS@cNF but without flashlight irradiation, where some dead bacteria were visible. To test the efficiency of this method, contact lenses after all treatments were washed and immersed in new LB-broth to visualize the growth of new bacteria to the solution from contact lenses. Figure 7d shows absorbance measured at 600 nm, commonly use to analyze the growth of bacteria.[83] The CL@D+ exhibited only a small amount of bacterial growth, slightly higher than the control (Clean CL), which corresponds with the direct test on the agar plate.

Using a method similar to that in the publication by Strojny-Cieślak et al. et al.,[84] we utilized PrestoBlue, a resazurin-based cell viability reagent used to assess the metabolic activity of bacteria, to measure the increase in fluorescence, which corresponds to high bacterial viability.[85] Measurement of fluorescence showed that treated contact lenses (CL@D+) had much lower fluorescence than untreated contact lenses (CL) (Figure 7e). This indicates that contact lenses treated with the deMS@cNF nanoplatform, and irradiation exhibited significantly reduced bacterial regrowth in the new solution.

To further examine the morphology of bacteria after irradiation, SEM analysis was conducted (Figure 7f). Control samples of contact lenses with bacteria (CL) showed bacterial cells on the surface with a clearly visible round shape. For the sample CL@D+, SEM images indicated destruction of bacterial cells by damaging the membrane and causing collapse (red arrows) (Figure 7f). The periostracum layer (PL) in deMS@cNF during the *in vitro* studies reached a temperature of 70-80°C immediately after flashlight irradiation, transferring heat to the contact lenses and damaging the bacterial membrane, thus leading to bacterial death.[12]

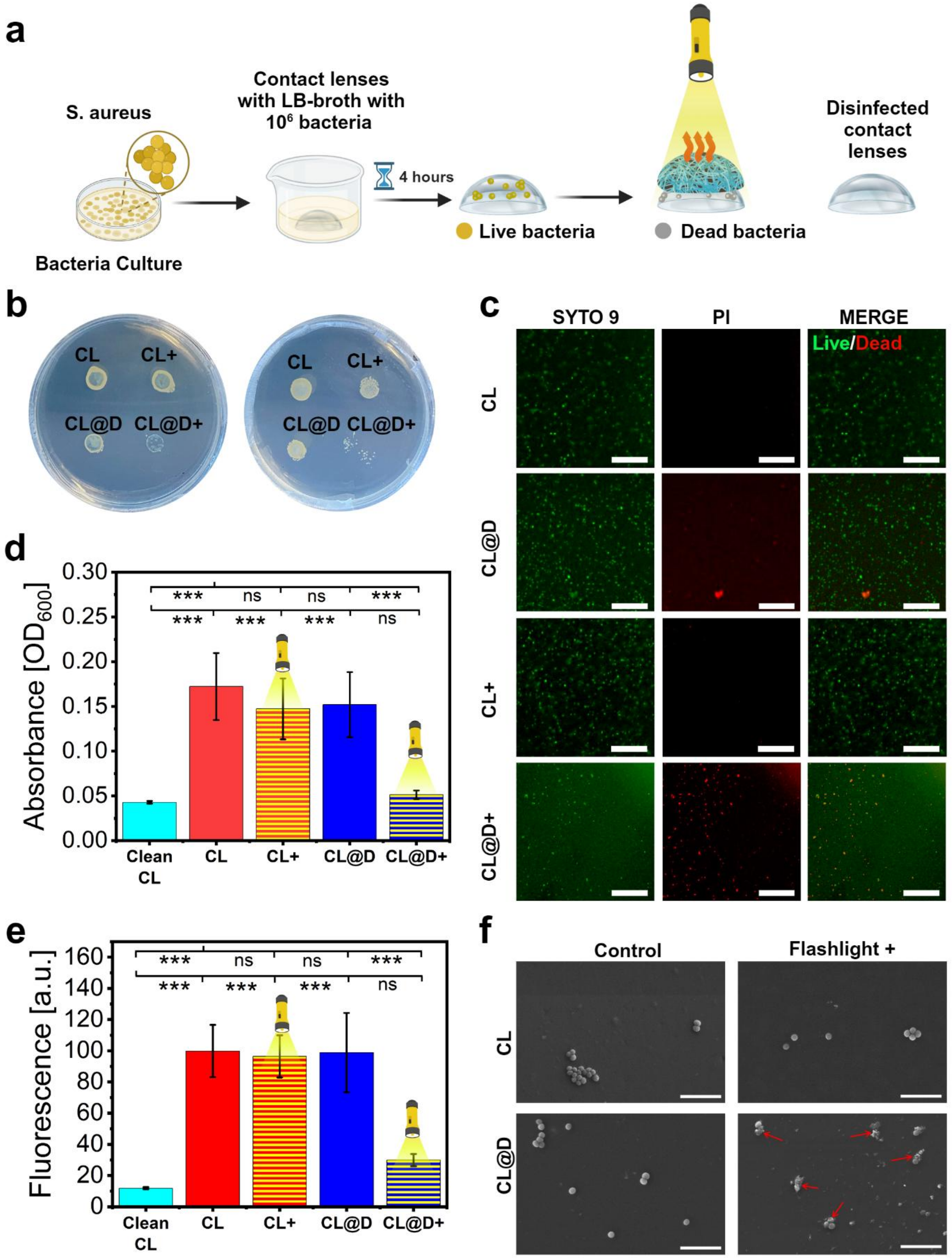

Figure 7. On demand antibacterial studies on contact lenses. a) Illustration of the application of the multifunctional nanoplatform (deMS@cNF) in effectively eradicating bacteria (*S.aureus*) from the surface of contact lenses. b) Agar plates showing imprints of irradiated and non-irradiated with and without deMS@cNF contact lenses. c) Confocal images with Live/Dead stain showing effective eradication upon the use of deMS@cNF with flashlight (Live bacteria

- green, Dead bacteria – red). Scale bar: 100 µm d) Optical density measured at 600 nm absorbance after immersing contact lenses overnight in fresh broth. e) Measurement of fluorescence for the PrestoBlue test performed on solutions after overnight soaking of contact lenses. f) SEM images of contact lens surfaces contaminated with bacteria before and after flashlight irradiation (+), both with (CL@D) and without (CL) deMS@cNF. Scale bar: 5 µm. Contact lenses (CL), Contact lenses irradiated with flashlight (CL+), Contact lenses cover with deMS@CNF (CL@D), Contact lenses with deMS@cNF irradiated with flashlight (CL@D+).

3. Conclusion

In this study, we developed and characterized a multifunctional nanoplatform derived from demineralized mussel shells and nanofibers enhanced with chitin nanofibrils (deMS@cNF). The platform exhibited remarkable photothermal properties and an innovative antibacterial system for surface disinfection. The demineralization of mussel shells resulted in a soft, flexible platform with an initial multilayer structure. Incorporating chitin nanofibrils into PVA/PEO nanofibers significantly enhanced the mechanical properties of electrospun nanofibers.

Analysis reveals that mussel shells exhibit excellent absorbance of visible light, attributed to the presence of eumelanin, which efficiently converts the absorbed light into heat. The entire nanoplatform demonstrated outstanding photothermal performance under a bike LED flashlight irradiation, rapidly increasing temperatures up to 95°C. The multilayered deMS@cNF nanoplatform did not exhibit cytotoxic effects in indirect and direct cell studies, suggesting its suitability for biomedical applications.

Most importantly, our study demonstrated that the multifunctional nanoplatform deMS@cNF, when activated by flashlight irradiation, eradicated bacterial colonization on contact lenses, specifically targeting *S. aureus*, one of the main bacteria responsible for bacterial keratitis infection. Through a series of experiments, we confirmed the nanoplatform's efficacy under portable bike LED light for contact lens decontamination. Lenses treated with deMS@cNF and subjected to flashlight irradiation exhibited a significant decrease in bacterial growth and viability. These effects are attributed to the rapid light-induced heating of the periostracum layer within deMS@cNF, which allows it to reach temperatures between 70-95°C, to effectively damage bacterial membranes.

In conclusion, findings underscore the potential of this novel nanoplatform for practical applications in antimicrobial treatments and other biomedical fields, providing a flexible, efficient, and non-toxic solution for photothermal therapy and surface disinfection. Notably, the use of demineralized mussel shells for photothermal eradication of bacteria represents a novel approach, as previous studies predominantly utilized cuttlefish ink for similar purposes. This innovation highlights the unique properties and advantages of mussel shells in developing effective antibacterial systems.

4. Experimental section

Materials

Chemicals and reagents used in this study were sourced from several suppliers. Polyvinyl alcohol (PVA) with an average molecular weight of 85,000-124,000 Da and a degree of hydrolysis of 99+%, poly(ethylene oxide) (PEO) with an average molecular weight of 1,000,000 Da stabilized with 200-500 ppm BHT, hexamethyldisilazane (HMDS), 100% acetic acid (AA), 37% hydrochloric acid, ethanol absolute, and 98.5% purity ethylenediaminetetraacetic acid (EDTA), along with sodium hydroxide, were all obtained from Sigma Aldrich. Phosphate buffered saline (PBS), triton X-100, and 4′,6-diamidino-2-phenylindole dihydrochloride (DAPI) were purchased from Roth. Dulbecco's modified eagle's medium (DMEM), fetal bovine serum (FBS), penicillin-streptomycin, and EDTA-Trypsin were provided by Gibco Invitrogen. Alexa Fluor 488 Phalloidin, Live/Dead™ Viability/Cytotoxicity Kit, PrestoBlue reagent, and Live/Dead™ BacLight™ Bacterial Viability Kits were supplied by Thermo Fisher Scientific. Lysogeny broth (LB) and lysogeny agar (LB Agar) were acquired from A&A Biotechnology. Staphylococcus aureus (S. aureus) ATCC 6538 was procured from Pol-AUR. SoftLens daily disposable contact lenses made of hilafilcon B by Bausch & Lomb.

Mussel-derived nanostructured platform material preparation

Demineralization of mussel shells

*M*ussel shells (*Mytilus edulis)* were obtained from a local seafood vendor at Hala Banacha market in Warsaw, Poland. To prepare them for further processing, the shells were first boiled for 15 minutes at 90°C to encourage opening. This allowed for easier removal of the soft tissue (mantle and visceral mass) inside the shells. Following dissection, the shells underwent ultrasonic cleaning for 30 minutes to remove any remaining debris or contaminants on their surfaces. After drying completely, all shells were precisely cut into uniform round shapes using a milling machine. The target diameter for these shapes was approximately 12 ± 2 mm and the target thickness was approximately 0.77 ± 0.12 mm. The demineralization process commenced using the method described by Ehrlich et al.[26] The prepared mussel shells (MS) were submerged in an EDTA solution.[26] For the preparation of this solution, EDTA powder (174 g/L) was gradually added to MilliQ water under continuous and vigorous stirring on a magnetic stirrer at room temperature. Since EDTA requires a pH ≥ 8 to dissolve, the pH of the solution was incrementally adjusted from 4.6 to 8 by the gradual addition of sodium hydroxide. After the EDTA was completely dissolved, the pH was lowered to 7.25 by gradually adding diluted hydrochloric acid. This demineralization step was conducted in an oven at a controlled temperature of 39°C. To ensure the complete removal of calcium carbonate minerals, the EDTA solution was replaced with a fresh solution every 24 hours. The entire demineralization process typically lasted for around 7 days, although the exact duration could vary depending on the initial thickness of each shell.

Chitin nanofibrils extraction

Squid pens from Loligo vulgaris were obtained locally, hydrated, and cleaned with distilled water and 70% ethanol before drying for storage. The preparation of chitin nanofibrils was previously detailed in Montroni et al. paper.[55] Briefly, squid pen de-proteination involved soaking 1 g of cleaned squid pens in 100 mL of a 10 mM HCl solution (pH 2) with 20 mg of pepsin at 37°C for 24 hours on a rocking table. After rinsing with distilled water, the pens were submerged in 100 mL of a 100 mM phosphate buffer (pH 7.6) with 20 mg of trypsin and processed for another 24 hours at 37°C on a rocking table. Protein removal was verified by the disappearance of UV absorption at 280 nm, indicating the loss of tryptophan residues, using a Varian Cary 300 Bio spectrophotometer. For β-chitin nano-fibril preparation, protein-free β-chitin, cut into 0.5 cm^2 pieces, was stirred in 100 mL of a 5.6 mM acetic acid solution (pH 3) for 72 hours at room temperature. This process produced a stable, transparent, homogeneous, and viscous dispersion of β-chitin nano-fibrils (CT), which remained stable for over six months.

Preparation of electrospun nanofibers enriched with chitin nanofibrils

To establish a sustainable and non-toxic method for fabricating nanofibers enhanced with chitin, we optimized the preparation of polyvinyl alcohol (PVA) and polyethylene oxide (PEO) solutions. Our objective was to explore different concentrations and combinations of PVA/PEO with acetic acid (AA) and chitin nanofibrils suspended in AA, suitable for electrospinning applications. The first solution (PVA/PEO) involved dissolving a 3:1 (w/w) mixture of PVA and PEO in MilliQ water to achieve a final concentration of 9.4% (w/v). The second solution (PVA/PEO/AA) utilized a similar approach, dissolving a 3:1 (w/w) PVA/PEO blend in a pre-mixed solution of MilliQ water and AA (pH 3) with a 2:1 (v/v) ratio with final concentration of 9.4% (w/v). The third solution (PVA/PEO/CT) employed the same 3:1 (w/w) PVA/PEO blend. However, dissolved in a pre-mixed solution of MilliQ water and suspension of 0,1% of chitin nanofibrils in acetic acid (pH 3), with a final concentration of 9.4% (w/v). All the solutions were then heated and stirred at 90°C for three hours to ensure complete dissolution. Subsequently, the solution was mix overnight to attain homogeneity. To improve spinnability, ethanol was added to each polymer mixture in a volume ratio of 1:9 immediately before electrospinning.

For the electrospinning procedure, each solution (PVA/PEO, PVA/PEO/AA, or PVA/PEO/CT) was loaded into a 1 mL syringe equipped with a 22G needle (internal diameter of 0.413 mm). The syringe was mounted on a syringe pump, dispensing the polymer solution at a flow rate of 400 µL/h. A high-voltage power supply set to 16 kV facilitated the formation of nanofibers, which were collected on a flat collector positioned 16 cm from the needle tip. The electrospinning was conducted under controlled ambient conditions.

Morphological characterization and physical-chemical characterization

Chitin nanofibril characterization

Nanofibers and chitin nanofibrils were imaged using a Field Emission Scanning Electron Microscopy (FE-SEM) (ZEISS Crossbeam 350 FIB-SEM microscope). Before imaging, nanofibers and chitin nanofibrils were sputtered with gold (2 × 2 × 2 min) in a DII-29030SCTR JEOL Smart Coater.

Fourier-transform infrared (FTIR) spectroscopy of chitin nanofibrils spectra were collected using a Nicolet iS10 spectrophotometer. Omnic software (Thermo Electron Corp., Woburn, MA) was used for data processing and baseline correction. The samples were prepared as KBr pellets and the sample concentration was 2 wt %. The spectra were obtained with 4 cm^{-1} resolution and 64 scans.

X-ray diffraction (XRD) patterns for chitin nanofibrils were collected using a PanAnalytical X'Pert Pro diffractometer equipped with a multi-array X'Celerator detector using Cu Kα radiation generated at 40 kV and 40 mA ($\lambda = 1.54056$ Å). The diffraction patterns were collected in the 2θ range between 4° and 25° with a step size ($\Delta 2\theta$) of 0.05° and a counting time of 100 s. Each pattern collection was repeated at least twice on different samples.

Evaluation of mussel shells and nanoplatform features

deMS and deMS@cNF for morphology preparation were first subsequently dehydrated with a series of increasing concentration of ethanol (50% once for 10 min; 75% once for 10 min; 90% once for 10 min; and 100%, twice for 10 min). Then the deMS and deMS@cNF were subsequently soaked in EtOH/HDMS solution (50% once for 10 min; 75% once for 10 min; 90% once for 10 min; and 100%, once and air dried).

Samples were imaged using a scanning electron microscope (SEM) (JSM-6010PLUS/LV, In TouchScope microscope). Depending on the sample, images were taken with different electron beam energies (7 to 12 kV) and magnifications. Before imaging, nanofibers and chitin nanofibrils were sputtered with gold (2 × 2 × 2 min) in a DII-29030SCTR JEOL Smart Coater.

Fourier transform infrared (FT-IR) analyses of mussel shell before and after demineralization were carried out in attenuated total reflectance (ATR) mode with a Bruker Vertex70 FT-IR spectrometer, and a wavenumber range of 400–4000 cm^{-1} was recorded with a resolution of 2 cm^{-1} after 10 scans for each sample.

The Raman spectra were acquired with LabRam HR800 Raman spectrometer (laser excitation: 532 nm for (PRL+NL)deMS, (PRL+NL)MS and 784 nm for (PL)deMS) (Horiba Jobin Yvon), with the observation of the Raman shifts in the range from 400 to 1700 cm^{-1}.

Mechanical characterization of electrospun nanofibers enriched with chitin nanofibrils

To investigate the influence of chitin nanofibrils on the mechanical properties of PVA/PEO nanofibers, we conducted a comprehensive evaluation of the tensile properties of PVA/PEO, PVA/PEO with AA, and PVA/PEO with chitin nanofibrils (CT) nanofibrous mats both before and after crosslinking. The evaluation employed a CTX texture analyzer (AMETEK Brookfield, US) equipped with a 5 N load cell, specifically adapted for handling thin and delicate samples. Rectangular strips of electrospun nanofibers measuring 10 mm by 40 mm were carefully mounted on the texture analyzer to ensure precise positioning and uniform stress distribution during testing. The thickness of each nonwoven sample was accurately measured using Kroeplin flat calipers, and an average value was computed for subsequent analyses. The crosshead speed of the testing device was maintained at a constant 1 mm/s. Through the analysis of the stress-strain curves derived from these tests, we determined critical mechanical parameters such as Young's Modulus. To ensure the reliability and reproducibility of the results, each formulation underwent three independent test repetitions. All tests were conducted on dry samples under standard ambient conditions.

Determination of glucosamine in electrospun nanofibers by HPLC

To analyze the amount of β-chitin incorporated in the nanofibers, we used the method described by Zhu et al.[69] 10 mg of sample were digested in 2.5 mL of 8 M HCl (purchased from Merck) at 110 °C for 4 h in a PYREX glass vial equipped with a Teflon coated cap. Then the solution was neutralized using NaOH 10 M and brought to 5 mL in a volumetric flask. The solution was then filtered on a 0.45 μm Teflon syringe filter and stored at -20 °C until it was analyzed.

Prior analyses, the sample was derivatized in an HPLC vial. 300 μL of a borate buffer 0.2 M at pH 7.0 were added in the vial, then 300 μL of a 0.5 mM fluorenylmethyloxycarbonyl chloride (FMOC-Cl) solution in acetonitrile, and finally 50 μL of sample. The sample was then incubated at least 30 min prior being analyzed.

The quantification was performed on the area of the chromatographic peak with retention time of 4.5 min. The calibration curve was done preparing standard solution by diluting a digested sample of pure β-chitin.

Nanoplatform-water relationship evaluation

Surface wettability assessments were conducted using a Data Physics OCA 15EC contact angle goniometer (Germany). This evaluation involved the measurement of water droplet contact angles on mussel shell samples before (MS) and after (deMS) demineralization. Each sample was precisely positioned on a microscope glass slide, and a 2 μL droplet of diH2O was deposited at room temperature. The contact angle was recorded at the 5-second mark post-application. To ensure reliability, this procedure was repeated three times per sample, allowing for consistent and reproducible data. The contact angle was measured using Origin Pro software with LBADSA plugin.[86]

The swelling ratio (SR) was determined by immersing accurately weighed deMS@cNF in MilliQ water until an equilibrium weight was reached. The samples were dried to a constant dry weight prior to the test. Changes in mass were recorded at predefined time intervals until no further weight change was observed. The SR was calculated using the following formula (equation 1):

$$SR = \frac{(W_d - W_f)}{W_f} * 100\% \qquad (1)$$

where W_d is the initial weight of the dry sample and W_f is the final weight of the sample at predefined time points.

The water content (WC) was measured by weighing the deMS@cNF before and after dehydration. The WC was calculated as follows (equation 3):

$$WC = \frac{(W_w - W_a)}{W_a} * 100\%) \qquad (2)$$

where W_w is the initial weight of the wet sample weight before dehydration and W_a is the final weight of the dry sample after dehydration sample at predefined time points.

Assessment of the photothermal properties

The photothermal properties of the deMS@cNF composite were evaluated using flashlight irradiation. A high-intensity flashlight (OFFBONDAGE HR3-1000) served as the irradiation source for the samples. To accurately capture and analyze the spatial heating distribution and temperature profiles induced by the flashlight, we utilized a high-resolution thermal camera (FLIR A655sc). This camera is equipped with FLIR ResearchIR Max software, which facilitates the recording and detailed analysis of the thermal data collected during the experiments. The power output of a flashlight across three distinct intensity levels was measured using the StarBright Color Advanced Laser Power & Energy Meter. Measurements were taken at various distances to determine the power for each flashlight setting. Spectra of flashlight were measured using HR4000 Spectrometer, Ocean Optics.

In vitro cell proliferation and viability

L929 murine fibroblast cells, sourced from Sigma-Aldrich, were cultured in medium (DMEM supplemented with 10% fetal bovine serum (FBS) and 1% penicillin/streptomycin (P/S)). The cultures were maintained at 37°C in a 5% CO_2 atmosphere. Once approximately 80% confluence was achieved, cells were trypsinized using a 0.05% EDTA-trypsin solution and subsequently centrifuged at 1200 rpm for 5 minutes. For direct assays, 10,000 cells were seeded per well of a 24-well plate in 1 ml of medium. For indirect assays, 5,000 cells were seeded per well of a 96-well plate in 200 µl of medium.

Direct cells seeding

The demineralized mussel shell embedded with crosslinked nanofibers (deMS@cNF) intended for direct study were immersed in 70% alcohol for 15 minutes and then washed with sterilized PBS five times. Next, the samples were sterilized using UV light, and treating them for 30 minutes on each side. The deMS@cNF (diameter ~ 1 cm) were then placed in a 24-well plate, and autoclaved titanium rings were added to the deMS@cNF samples to keep them at the bottom of the wells. Then, cells were directly seeded onto the deMS@cNF nanoplatform at a density of 10,000 cells per well of a 24-well plate in 1 ml of medium. In parallel, cells were also seeded onto round slide glass as a control. In parallel, cells were also seeded onto round slide glass as a control. Medium changes were carried out on 3 day over a period of 7 days.

Indirect cells seeding

For the indirect testing, based on ISO 10993-12:2021 standards, examine the impact of the released molecules from deMS@cNF on cell survival and proliferation.[87,88] The sample extracts from deMS@cNF nanoplatform were prepared as follows: deMS@cNF samples were weighted to match the 0.2 g/ml standard extraction ratio.[88] Samples were sterilized using an autoclave. After sterilization were in media for 24 hours at 37°C in a 5% CO_2 atmosphere. The resultant extracts were then filtered through a 0.2μm filter for secondary sterilization. L929 fibroblasts were seeded at 5,000 cells per well of a 96-well plate in 200 μl of medium. The next day, the medium was replaced with extracts of deMS@cNF for the experimental wells, while the control wells retained the original medium.

Viability assay

Cell viability was quantitatively measured using the PrestoBlue assay on days 1, 3, and 7 of culture for indirect method. Each sample and control, in quintuplicates, were treated with a 10% (v/v) solution of PrestoBlue reagent in culture medium. After 2 hours of incubation at 37°C in 5% CO_2, 100 μL aliquots from triplicates were transferred to a 96-well plate, and fluorescence was measured at 530 nm excitation and 620 nm emission using a Fluoroskan Ascent™ Microplate Fluorometer by Thermo Scientific.

On days 3 and 7, a Live/Dead assay was performed to evaluate cell viability and detect potential cytotoxic effects from the materials. Cells were stained using a solution of 0.5 μL calcein and 2 μL ethidium homodimer in 1 mL PBS, incubated for 10 minutes, washed three times with PBS, and imaged using a Leica TCS SP5 X confocal microscope.

Morphology evaluation

For direct tests, cell morphology on samples was analyzed using SEM. Samples were fixed in 3% glutaraldehyde (GTA) for 3 hours at ice-cold temperatures, washed three times in DI water, and dehydrated in graded ethanol solutions for 15 minutes each step. After dehydration, HMDS was applied, and samples were left to air-dry under a fume hood. Samples were then sputter-coated were sputtered with gold (2 × 2 × 2 min) in a DII-29030SCTR JEOL Smart Coater and examined using SEM (JSM-6010PLUS/LV, In TouchScope microscope).

For indirect tests, after initial PBS washes, cells were fixed in 4% paraformaldehyde for 15 minutes at room temperature. Post-fixation, cells underwent a permeabilization step in 0.3% Triton X-100 for 15 minutes, followed by blocking in 1% BSA with 0.1% Triton X-100 for 30 minutes. Cells were then stained with 1:40 Alexa Fluor 488 Phalloidin and 1:500 DAPI in PBS, each for 40 minutes and 10 minutes respectively, in darkness. After a final wash, the cytoskeleton and nuclei were visualized under a confocal microscope.

In Vitro **assessment of the on-demand antibacterial properties**

To evaluate the antimicrobial properties of the contact lenses, *Staphylococcus aureus* strains were cultured in Lysogeny Broth (LB) for 24 hours at 37°C in a shaker incubator. Contact lenses were removed from their original packaging and cut into smaller round pieces with a diameter of 6 mm. The contact lenses were placed in 96-well plates, and each well was inoculated with 200 µL of a bacterial solution (1.0×10^6 cfu/mL). For control wells, only LB-broth was added. The plates were shaken for 15 minutes to ensure uniform distribution of the bacteria and then incubated at 37°C for 4 hours. Post-incubation, the plates were removed for further processing to assess the effects of photothermal treatment using the deMS@cNF sample and flashlight irradiation on bacterial growth on the lens surfaces.

Absorbance measurement at OD 600 nm

The optical density (OD) at 600 nm was measured to assess bacterial growth quantitatively. Following treatment (irradiation with a flashlight or exposure to deMS@cNF), the contact lenses were washed with 0.1 M PBS and transferred to a fresh 96-well plate. Then, 250 µL aliquots of LB medium were added to the wells containing the contact lenses (both control and treated). After the respective treatments and a further 24-hour incubation with new LB broth, 100 µL from each well was transferred to a new plate. The absorbance at 600 nm was measured using a UV-Vis spectrophotometer. This measurement provides an indirect quantification of the bacterial biomass in each well, allowing for an evaluation of the growth inhibition caused by the multilayered nanoplatform and LED flashlight.

Quantification of bacterial viability using PrestoBlue

To quantitatively assess the bactericidal efficacy of the deMS@cNF with flashlight treatment, PrestoBlue cell viability reagent was used as described elsewhere.[84] Following treatment (irradiation with a flashlight or exposure to deMS@cNF) the contact lenses were washed with 0.1 M PBS and transferred to a fresh 96-well plate. Then, 250 µL aliquots of LB medium were added to the wells containing contact lenses (both control and treated). After incubation for 24 hours, 90 µl of bacteria suspensions (with or without flashlight irradiation and with and without deMS@cNF) were transferred to 96-well plates. 10 µL of PrestoBlue reagent was added to each well containing the bacterial cultures. The plates were then incubated at 37°C for 20 min. The fluorescence intensity, indicating bacterial viability, was measured using a fluorescence microplate reader at an excitation wavelength of 560 nm and an emission wavelength of 590 nm.

Verification of the antibacterial effect by direct contact method

The antibacterial efficacy of both flashlight-irradiated and non-irradiated contact lenses, as well as those coated with deMS@cNF, was assessed using the direct contact method. Immediately following irradiation or post-cultivation, the lenses were rinsed with sterile 0.1 M PBS and aseptically transferred onto solid LB agar plates. Each sample was gently pressed against the agar for 30 seconds and then removed. This procedure was replicated, leaving some lenses on the agar to enhance bacterial transfer. The plates were then incubated at 37°C for 24 hours and subsequently photographed to document bacterial growth.

Live/Dead bacteria staining and confocal microscopy analysis

To further assess the cytotoxic effects and the viability of bacterial cells following irradiation with a flashlight or exposure to deMS@cNF, Live/Dead BacLight Bacterial Viability staining was utilized. This method employs a combination of SYTO 9 green, fluorescent nucleic acid stain, which labels all dead and live bacteria, and propidium iodide, which labels dead bacteria. Samples treated with the deMS@cNF/Flashlight (CL@D+, CL+) and controls (CL@D, CL) were stained according to the manufacturer's instructions. Briefly, after the treatment samples were rinsed with sterile 0.1 M phosphate-buffered saline (PBS) and then stained with 10 µl SYTO 9 green + 10 µl of PI and were incubated in the dark at room temperature for 15 minutes, allowing adequate time for staining. Following staining, the samples were examined under a confocal laser scanning microscope. Confocal images were captured to assess the distribution of live and dead bacteria across the treated surfaces. This analysis provides detailed insights into the efficacy of the disinfection method.

Evaluation of morphology of bacteria on contact lenses

The morphology of biofilms on non-irradiated and irradiated contact lenses, including those coated with deMS@cNF, was examined using SEM. All samples were fixed in 9% paraformaldehyde at room temperature for 60 minutes, rinsed with sterile 0.1 M PBS, and then deionized water. The fixed samples were stored at -20°C until SEM analysis. Prior to imaging, the samples were thawed and subjected to a dehydration sequence in ethanol solutions of increasing concentration (25%, 50%, 70%, 90%, 100%). Finally, samples were then sputter-coated were sputtered with gold (2 × 2 × 2 min) in a DII-29030SCTR JEOL Smart Coater and examined using SEM (JSM-6010PLUS/LV, In TouchScope microscope).

Statistical analysis

The tests were performed at least in $n \geq 3$ repetitions. All data were presented as mean ± standard deviation (SD). A one-way analysis of variance (ANOVA) and an analysis of variances (Turkey`s test) were used to determine differences (p-value ≤ 0.05: $^{*}p \leq 0.05$, $^{**}p \leq 0.01$, $^{***}p \leq 0.001$).

Supporting Information

Supporting information is available from the Wiley Online Library or from the author.

Acknowledgements

This work was supported by the National Science Centre (NCN) SONATA BIS Project No. 2020/38/E/ST5/00456. Figures 1, 2, 3, 4, 5, 6, and 7 were partially created using BioRender. Parts of Figures 1, 3, 5, and 7 were used from free-licensed resources Freepik.com. We would like to thank Anna Zakrzewska for performing the FE-SEM imaging.

Conflict of Interest

The authors declare no conflict of interest.

Received: ((will be filled in by the editorial staff))
Revised: ((will be filled in by the editorial staff))
Published online: ((will be filled in by the editorial staff))

References

[1] Y. H. Aldebasi, M. Salah, M. I. Aly, Ahmad, Y. Homood, **2013**.

[2] W. L. Johnson, M. Sohn, C. F. Woeller, R. A. F. Wozniak, *Invest. Ophthalmol. Vis. Sci.* **2023**, *64*, 5.

[3] S. A. Khan, C.-S. Lee, *Acta Biomater.* **2020**, *113*, 101.

[4] A. Mordmuang, L. Udomwech, K. Karnjana, *Clin. Ophthalmol.* **2021**, *15*, 2391.

[5] E. Iyamu, F. O. Ekhaise, *Jrnl Nig Opto Assoc.* **2021**, *23*, 25.

[6] M. M. Gabriel, C. McAnally, H. Chen, S. Srinivasan, V. Manoj, R. Garofalo, *OPTO.* **2021**, *13*, 7.

[7] L. B. Szczotka-Flynn, Y. Imamura, J. Chandra, C. Yu, P. K. Mukherjee, E. Pearlman, M. A. Ghannoum, *Cornea* **2009**, *28*, 918.

[8] M. Mohammadinia, S. Rahmani, G. Eslami, M. Ghassemi-Broumand, M. Aghazadh Amiri, G. Aghaie, S. M. Tabatabaee, S. Taheri, A. Behgozin, *Eye* **2012**, *26*, 327.

[9] C. K. M. Choy, P. Cho, M. V. Boost, *Clin. Exp. Optom.* **2012**, *95*, 198.

[10] K. Hoenes, U. Wenzel, M. Hessling, *Biomed Tech (Berl)* **2020**, *65*, 485.

[11] K. Hoenes, B. Spellerberg, M. Hessling, *Int. J. Environ. Res. Public Health* **2020**, *17*, DOI 10.3390/ijerph17176422.

[12] Y. Zhao, Y. Wang, X. Wang, R. Qi, H. Yuan, *Nanomaterials (Basel)* **2023**, *13*, DOI 10.3390/nano13152269.

[13] B. Alkan-Taş, E. Berksun, C. E. Taş, S. Ünal, H. Ünal, *Progress in Organic Coatings* **2022**, *164*, 106669.

[14] J. L. Vidal, T. Jin, E. Lam, F. Kerton, A. Moores, *Current Research in Green and Sustainable Chemistry* **2022**, *5*, 100330.

[15] N. Yan, X. Chen, *Nature* **2015**, *524*, 155.

[16] S. Ngasotter, K. A. M. Xavier, M. M. Meitei, D. Waikhom, Madhulika, J. Pathak, S. K. Singh, *Carbohydrate Polymer Technologies and Applications* **2023**, *6*, 100349.

[17] B. Terkula Iber, N. Azman Kasan, D. Torsabo, J. Wese Omuwa, *j. renew. mater.* **2022**, *10*, 1097.

[18] S. Ifuku, H. Saimoto, *Nanoscale* **2012**, *4*, 3308.

[19] N. A. N. Dzolkifle, W. M. F. Wan Nawawi, *Int. J. Biol. Macromol.* **2024**, *265*, 130858.

[20] M. Kozma, B. Acharya, R. Bissessur, *Polymers (Basel)* **2022**, *14*, DOI 10.3390/polym14193989.

[21] B.-M. Min, S. W. Lee, J. N. Lim, Y. You, T. S. Lee, P. H. Kang, W. H. Park, *Polymer* **2004**, *45*, 7137.

[22] I. P. Dobrovolskaya, I. O. Lebedeva, V. E. Yudin, P. V. Popryadukhin, E. M. Ivan’kova, V. Yu. Elokhovskii, *Polym. Sci. Ser. A* **2016**, *58*, 246.

[23] I. P. Dobrovolskaya, V. E. Yudin, P. V. Popryadukhin, E. M. Ivan’kova, A. S. Shabunin, I. A. Kasatkin, P. Morgantie, *Carbohydr. Polym.* **2018**, *194*, 260.

[24] J. Junkasem, R. Rujiravanit, P. Supaphol, *Nanotechnology* **2006**, *17*, 4519.

[25] X. Song, J. Mei, X. Zhang, L. Wang, G. Singh, M. M. Q. Xing, X. Qiu, *Biomater. Sci.* **2017**, *5*, 1101.

[26] H. Ehrlich, R. Martinović, D. Joksimović, I. Petrenko, S. Schiaparelli, M. Wysokowski, D. Tsurkan, A. L. Stelling, A. Springer, M. Gelinsky, A. Joksimović, *Appl. Phys. A* **2020**, *126*, 562.

[27] M. H. Azarian, W. Sutapun, *Front. Mater.* **2022**, *9*, DOI 10.3389/fmats.2022.1024977.

[28] M. Barbachi, M. El Biriane, M. Bouabaz, K. Boudjellal, *Applied Journal of Environmental Engineering Science* **2019**, DOI 10.48422/imist.prsm/ajees-v5i2.16422.

[29] M. Alm, R. Tauson, H. Wall, *J. Appl. Poult. Res.* **2016**, pfw056.

[30] R. Martinović, D. Joksimović, A. Perošević-Bajčeta, I. Čabarkapa, H. Ehrlich, *Appl. Sci.* **2023**, *13*, 7582.

[31] S. Derkach, V. Salnikov, P. Kravets, O. Tyukina, A. Glukharev, Y. Zuev, Y. Kuchina, *E3S Web of Conferences* **2023**, *460*, 01006.

[32] S. Affenzeller, K. Wolkenstein, H. Frauendorf, D. J. Jackson, *Front. Zool.* **2019**, *16*, 47.

[33] L. Guo, W. Li, Z. Gu, L. Wang, L. Guo, S. Ma, C. Li, J. Sun, B. Han, J. Chang, *Int. J. Mol. Sci.* **2023**, *24*, DOI 10.3390/ijms24054360.

[34] A. Bl 罿 quez-Castro, J. Carlos Stockert, *Biocell* **2021**, *45*, 849.

[35] X. Kong, H. Chen, F. Li, F. Zhang, Y. Jiang, J. Song, Y. Sun, B. Zhao, J. Shi, *Int. J. Biol. Macromol.* **2023**, *237*, 124176.

[36] Y. Liang, Y. Zhao, H. Sun, J. Dan, Y. Kang, Q. Zhang, Z. Su, Y. Ni, S. Shi, J. Wang, W. Zhang, *Food Chem.* **2023**, *401*, 134117.

[37] X. Cao, L. Sun, D. Xu, S. Miao, N. Li, Y. Zhao, *Adv Sci (Weinh)* **2023**, *10*, e2300902.

[38] Q. Lei, D. He, L. Ding, F. Kong, P. He, J. Huang, J. Guo, C. J. Brinker, G. Luo, W. Zhu, Y. Yu, *Adv. Funct. Mater.* **2022**, *32*, DOI 10.1002/adfm.202113269.

[39] Q. Jia, Z. Fu, Y. Li, Z. Kang, Y. Wu, Z. Ru, Y. Peng, Y. Huang, Y. Luo, W. Li, Y. Hu, X. Sun, J. Wang, Z. Deng, C. Wu, Y. Wang, X. Yang, *ACS Appl. Mater. Interfaces* **2024**, *16*, 13422.

[40] Y. M. Liu, W. S. Ma, Y. X. Wei, Y. H. Xu, *Biomed. Environ. Sci.* **2020**, *33*, 471.

[41] B. P. Bourgoin, *Mar. Environ. Res.* **1988**, *25*, 125.

[42] Z. Liao, L. Bao, M. Fan, P. Gao, X. Wang, C.-L. Qin, X.-M. Li, *J. Proteomics* **2015**, *122*, 26.

[43] M. Suzuki, T. Kogure, H. Nagasawa, *AGri-Biosci. Monogr. (AGBM)* **2017**, *7*, 25.

[44] P. Gao, Z. Liao, X.-X. Wang, L.-F. Bao, M.-H. Fan, X.-M. Li, C.-W. Wu, S.-W. Xia, *PLoS ONE* **2015**, *10*, e0133913.

[45] W. Dong, J. Huang, C. Liu, H. Wang, G. Zhang, L. Xie, R. Zhang, *Front. Mar. Sci.* **2022**, *9*, DOI 10.3389/fmars.2022.862929.

[46] P. Mohammadi, W. Wagermaier, M. Penttilä, M. B. Linder, **2021**, DOI 10.20944/preprints202102.0037.v1.

[47] X. Feng, R. Gao, R. Wang, G. Zhang, *CrystEngComm* **2020**, *22*, 3100.

[48] E. Ferraz, J. A. F. Gamelas, J. Coroado, C. Monteiro, F. Rocha, *Waste Biomass Valor.* **2019**, *10*, 2397.

[49] J. Harris, I. Mey, M. Hajir, M. Mondeshki, S. E. Wolf, *CrystEngComm* **2015**, *17*, 6831.

[50] K. Ramesh, F. Melzner, A. W. Griffith, C. J. Gobler, C. Rouger, D. Tasdemir, G. Nehrke, *J. R. Soc. Interface* **2018**, *15*, DOI 10.1098/rsif.2017.0723.

[51] S. Derkach, P. Kravets, Y. Kuchina, A. Glukharev, O. Tyukina, V. Bordiyan, Y. Alloyarova, P. Priymak, S. Malavenda, O. Zueva, D. Kolotova, *Food Biosci.* **2023**, *56*, 103188.

[52] G. Cárdenas, G. Cabrera, E. Taboada, S. P. Miranda, *J. Appl. Polym. Sci.* **2004**, *93*, 1876.

[53] Y. Ogawa, C. M. Lee, Y. Nishiyama, S. H. Kim, *Macromolecules* **2016**, *49*, 7025.

[54] S.-H. Jeong, J.-K. Kim, Y.-W. Lim, H.-B. Hwang, H.-Y. Kwon, B.-S. Bae, J. Jin, *APL Mater.* **2018**, *6*, 016102.

[55] D. Montroni, B. Marzec, F. Valle, F. Nudelman, G. Falini, *Biomacromolecules* **2019**, *20*, 2421.

[56] Y. Fan, T. Saito, A. Isogai, *Biomacromolecules* **2008**, *9*, 1919.

[57] P. Lertwattanaruk, N. Makul, C. Siripattarapravat, *J. Environ. Manage.* **2012**, *111*, 133.

[58] Q. Wu, E. Jungstedt, M. Šoltésová, N. E. Mushi, L. A. Berglund, *Nanoscale* **2019**, *11*, 11001.

[59] S. Suenaga, N. Nikaido, K. Totani, K. Kawasaki, Y. Ito, K. Yamashita, M. Osada, *Int. J. Biol. Macromol.* **2016**, *91*, 987.

[60] G. Cabrera-Barjas, C. González, A. Nesic, K. P. Marrugo, O. Gómez, C. Delattre, O. Valdes, H. Yin, G. Bravo, J. Cea, *Mar. Drugs* **2021**, *19*, DOI 10.3390/md19040184.

[61] K. VANDEVELDE, P. KIEKENS, *Carbohydr. Polym.* **2004**, *58*, 409.

[62] L. A. Rodrigues, I. Radojčić Redovniković, A. R. C. Duarte, A. A. Matias, A. Paiva, *ACS Omega* **2021**, *6*, 28729.

[63] C. McReynolds, A. Adrien, N. B. de Fraissinette, S. Olza, S. C. M. Fernandes, *Biomass Conv. Bioref.* **2022**, DOI 10.1007/s13399-022-03569-9.

[64] Z. Renkler, I. Cruz Maya, V. Guarino, *Fibers* **2023**, *11*, 85.

[65] N. Z. Al-Hazeem, N. M. Ahmed, *ACS Omega* **2020**, *5*, 22389.

[66] A. Zakrzewska, S. S. Zargarian, C. Rinoldi, A. Gradys, D. Jarząbek, M. Zanoni, C. Gualandi, M. Lanzi, F. Pierini, *ACS Mater. Au* **2023**, DOI 10.1021/acsmaterialsau.3c00025.

[67] M. B. Stie, M. Jones, H. O. Sørensen, J. Jacobsen, I. S. Chronakis, H. M. Nielsen, *Carbohydr. Polym.* **2019**, *215*, 253.

[68] T. H. N. Vu, S. N. Morozkina, M. V. Uspenskaya, R. O. Olekhnovich, in *2022 IEEE-EMBS Conference on Biomedical Engineering and Sciences (IECBES)*, IEEE, **2022**, pp. 344–349.

[69] X. Zhu, J. Cai, J. Yang, Q. Su, *Carbohydr. Res.* **2005**, *340*, 1732.

[70] E. Di Mauro, M. Camaggi, N. Vandooren, C. Bayard, J. De Angelis, A. Pezzella, B. Baloukas, R. Silverwood, A. Ajji, C. Pellerin, C. Santato, *Polym. Int.* **2019**, *68*, 984.

[71] J. C. Stockert, *InVet* **2021**.

[72] M. L. Terranova, E. Tamburri, *Polymer* **2021**, 123952.

[73] H. Chen, Y. Cheng, C. I. Moraru, *Sci. Rep.* **2023**, *13*, 15472.

[74] L. Wen, H. Wanpei, L. Qian, L. Xu, C. Rongsheng, N. Hongwei, Z. Weiting, *J. Mater. Sci.* **2020**, *55*, 9538.

[75] C. Chui, K. Hiratsuka, A. Aoki, Y. Takeuchi, Y. Abiko, Y. Izumi, *Lasers Surg. Med.* **2012**, *44*, 856.

[76] A. Lipovsky, Y. Nitzan, A. Gedanken, R. Lubart, *Lasers Surg. Med.* **2010**, *42*, 467.

[77] Y. Takeuchi, A. Aoki, K. Hiratsuka, C. Chui, A. Ichinose, N. Aung, Y. Kitanaka, S. Hayashi, K. Toyoshima, T. Iwata, S. Arakawa, *Antibiotics (Basel)* **2023**, *12*, DOI 10.3390/antibiotics12121676.

[78] A. Lipovsky, Y. Nitzan, H. Friedmann, R. Lubart, *Photochem. Photobiol.* **2009**, *85*, 255.

[79] R. Lubart, A. Lipovski, Y. Nitzan, H. Friedmann, *Laser Ther.* **2011**, *20*, 17.

[80] R. A. Ganz, J. Viveiros, A. Ahmad, A. Ahmadi, A. Khalil, M. J. Tolkoff, N. S. Nishioka, M. R. Hamblin, *Lasers Surg. Med.* **2005**, *36*, 260.

[81] J. S. Guffey, J. Wilborn, *Photomed. Laser Surg.* **2006**, *24*, 684.

[82] M. Rosenberg, N. F. Azevedo, A. Ivask, *Sci. Rep.* **2019**, *9*, 6483.

[83] H. Haase, L. Jordan, L. Keitel, C. Keil, B. Mahltig, *PLoS ONE* **2017**, *12*, e0188304.

[84] B. Strojny-Cieślak, S. Jaworski, M. Wierzbicki, M. Pruchniewski, M. Sosnowska-Ławnicka, J. Szczepaniak, A. Lange, P. Koczoń, M. Zielińska-Górska, E. S. Chwalibóg, *Environ. Sci. Pollut. Res. Int.* **2023**, DOI 10.1007/s11356-023-30151-1.

[85] N. Lall, C. J. Henley-Smith, M. N. De Canha, C. B. Oosthuizen, D. Berrington, *Int. J. Microbiol.* **2013**, *2013*, 420601.

[86] A. F. Stalder, T. Melchior, M. Müller, D. Sage, T. Blu, M. Unser, *Colloids and Surfaces A: Physicochemical and Engineering Aspects* **2010**, *364*, 72.

[87] In *ANSI/AAMI/ISO 10993-12:2012; Biological Evaluation of Medical Devices — Part 12: Sample Preparation and Reference Materials*, AAMI, **2012**.

[88] L. Szymanski, K. Golaszewska, A. Wiatrowska, M. Dropik, P. Szymanski, B. Gromadka, P. Krakowiak, J. Wierzchowska, D. Matak, *Biomater. Res.* **2022**, *26*, 12.

This study introduces a portable, eco-friendly method for disinfecting contact lenses using a light-activated nanoplatform. Developed from demineralized mussel shells and chitin nanofibrils, the multilayered nanoplatform uses a bike LED flashlight to rapidly heat and eliminate bacterial contamination on contact lens surfaces. *In vitro* tests confirm its biocompatibility and non-toxicity, providing a safe solution for lens disinfection.

*Magdalena Bartolewska, Alicja Kosik-Kozioł, Zbigniew Korwek, Devis Montroni, Maciej Mazur, Giuseppe Falini and Filippo Pierini**

Title: Eumelanin-Enhanced Photothermal Disinfection of Contact Lenses Using a Sustainable Marine Nanoplatform.

ToC figure